Detailed relationship between local structure, polarons, and magnetization for $La_{1-x}Ca_xMnO_3$ $(0.21 \leq x \leq 0.45)$

F. Bridges,[1] L. Downward,[1] J. J. Neumeier,[2] and T. A. Tyson[3]
[1]*Physics Department, University of California, Santa Cruz, California 95064, USA*
[2]*Department of Physics, Montana State University, Bozeman, Montana 59717, USA*
[3]*Department of Physics, New Jersey Institute of Technology, Newark, New Jersey 07102, USA*
(Received 20 January 2010; published 3 May 2010)

We present detailed local structure measurements (using the extended x-ray absorption fine structure technique) for the colossal magnetoresistive material $La_{1-x}Ca_xMnO_3$ $(0.21<x<0.45)$ as a function of temperature and magnetic field. The local distortions of the Mn-O bonds are parameterized using σ, the width of the Mn-O pair-distribution function (PDF). After subtracting thermal phonon contributions, we show that the contributions to σ^2 from polaron and Jahn-Teller (JT) distortions, $\sigma^2_{JT/polaron}$, are a *universal* function of the magnetization, independent of how the magnetization is achieved via changes in temperature or magnetic field. However this universal behavior is only observed for B fields ≥ 2 T, likely as a result of domain canting in low B fields. The resulting curve is well described by two straight lines with significantly different slopes. These regimes represent two distinctly differ distortions of the oxygen octahedra about the Mn. For low magnetizations up to ~65% of the theoretical maximum magnetization, M_T, the slope is low and the distortion removed as the sample becomes magnetized is small—we argue this arises from polarons which have a low distortion around two (or possibly three) Mn sites. At high magnetizations large distortions per Mn site are removed as these sites become magnetized. The data are also analyzed in terms of a two Mn-O peak distribution using experimental standards for Mn-O. The results agree well with recent neutron PDF results but not with some earlier results. We discuss the limitations of assuming a two peak distribution in view of the two distortions needed to describe the Mn-O distortions as a function of T and B for $B \geq 2$ T. It is likely that there is a distribution of longer bonds. Finally we show that with increasing B field, the Mn-Mn peak also has a small B-field-induced change—a measure at the unit cell level of magnetostriction but find that there is no observable B-field-induced change in the Mn-La/Ca pair distribution for fields up to ~10 T.

DOI: 10.1103/PhysRevB.81.184401 PACS number(s): 71.38.−k, 61.05.cj, 71.27.+a, 75.47.Lx

I. INTRODUCTION

Since the discovery of "colossal" magnetoresistance (CMR),[1] there has been extensive interest in manganites such as $La_{1-x}Ca_xMnO_3$ (LCMO). Although the end compounds $LaMnO_3$ and $CaMnO_3$ are antiferromagnetic (AFM), the CMR manganites are ferromagnetic (FM), and exhibit metallic conductivity in the FM phase, with a metal-insulator transition close to the FM transition temperature T_c.[2–4] For LCMO, CMR is observed over the concentration range, approximately $0.2<x<0.5$.[2,5]

The generally accepted ferromagnetic coupling mechanism in the manganites is called "double exchange" (DE), first introduced by Zener[6] and later expanded by others.[7,8] In Zener's original model he explicitly assumed that no lattice distortions were present and such distortions were also initially ignored by others. However, in the mid 1990s it was proposed that Jahn-Teller (JT) distortions must play a role to explain the large change observed in the CMR.[9–12] It is well known that $LaMnO_3$ has a large JT distortion—the Mn^{+3} ion has one e_g electron and hence is JT active with roughly four shorter bonds and two longer bonds.[13,14] In contrast, the Mn^{+4} ion in $CaMnO_3$ has no e_g electron and no JT distortions;[15] the six Mn-O bonds are nearly equal, within ± 0.01 Å. A crucial question is—what happens in the doped crystal $La_{1-x}Ca_xMnO_3$, which naïvely one might think of as a mixture of Mn^{+3} and Mn^{+4} sites? The holes introduced by Ca doping form polarons but the nature of this polaron is still not well defined—how many sites it covers and the distortions of those sites has not been explored in detail.

Over the last decade, many authors have observed significant local structure changes in the Mn-O pair distribution as a function of temperature using both extended x-ray absorption fine structure (EXAFS) spectroscopy[16–25] and neutron or x-ray pair-distribution function (PDF) analysis.[26–30] These investigations show that within the CMR regime, the average JT distortions at low T are very small (~0 for some samples), but grow rapidly as T approaches T_c. Above T_c the average JT distortions are constant. Within a two-peak fit of the Mn-O distribution there are different, inconsistent reports as to the length of the long Mn-O bonds.[21,29,30] (We will revisit this two-peak model using experimental EXAFS standards for the Mn-O pair.)

In addition to the observed CMR near T_c, the manganites also exhibit magnetostriction (a change in the unit-cell size in an applied field) over a comparable temperature range around T_c.[31–37] Early EXAFS studies[38–41] have also shown a small B-field-induced change in the Mn-O distortion at 1 T but the effect is too small at 1 T to explore the field dependence in depth.

Our first detailed study of the local structure as a function of applied B field up to ~10 T, considered only two concentrations 0.21 and 0.3 (Ref. 24) and suggested that there is a nearly universal relationship between the excess (nonthermal) broadening of the Mn-O pair distribution function ($\sigma_{JT/polaron}$ is this excess width) and the sample magnetiza-

tion. Here, we present a detailed EXAFS study as a function of temperature and magnetic field (up to ~10 T) over the CMR range for $La_{1-x}Ca_xMnO_3(0.21 \leq x \leq 0.45)$. These results now show a completely universal relationship between the nonphonon Mn-O local disorder and magnetization; that is, we will show that $\sigma^2_{JT/polaron}$ only depends on the fraction of magnetized sites, M/M_T, where M_T is the maximum magnetization. This functional relationship between $\sigma^2_{JT/polaron}$ and M/M_T is independent of how the magnetization is produced, either by lowering the temperature or by applying an external magnetic field, or both. Note however that to have magnetization saturation (i.e., no canting of local domains) such that M is a measure of all the magnetized sites, requires a B field above approximately 0.4 T.[24,42] Consequently this universality *only* exists for high B fields—for the measurements we have made, for $B \geq 2$ T.

Dimeron model

The plots of $\sigma^2_{JT/polaron}$ vs M discussed in Sec. III on page 8 show clearly that there are two distinct types of local distortion that exist near and above T_c, as reported earlier.[24] We associate the smaller of these local distortions with the mobile polarons for temperatures at which some JT distortions still exist, and refer to this type of polaron as a "dimeron;"[24] this model is described in more detail here. Although it likely will need to be revised/modified, it is a useful working model, as it has many of the local structure features that we observe in our data and is also consistent with a few other measurements. JT distortions have been considered in many theoretical calculations, but a low distortion, two-site quasiparticle (polaron) has not been explicitly included to our knowledge.

Consider $La_{0.70}Ca_{0.30}MnO_3$ above T_c as an example; 70% of the Mn sites are occupied by one e_g electron while e_g orbitals on 30% of the Mn sites must be vacant. Also, because of the large Hubbard U and Hund's rule coupling, double occupation of the t_{2g} and e_g orbitals is prohibited. If hopping were very slow and only distorted (1 e_g electron—Mn^{+3}) or undistorted (no e_g electron—Mn^{+4}) sites existed, the distorted sites would have a large JT splitting while the undistorted sites would have no JT splitting. Then the difference in JT energies forms a very large barrier for activated hopping. When an electron on occupied (distorted) site 1, hops to a vacant (undistorted) site, 2, the now occupied site 2 begins to distort, while site 1 which is now vacant, begins to undistort. The relaxation of the O positions about the Mn sites take place rapidly, on optical phonon time scales—$\sim 10^{-13}$ s; the electron states follow adiabatically. As the two Mn sites relax toward their new equilibrium local structures (one distortion increasing the other decreasing), the JT distortions about each site may become comparable. Then the two sites would have approximately the same JT energies, there would be little or no energy barrier for hopping between the sites, and electron hopping between them would be very fast. There will be some small quasiequilibrium distortion on each site. A cartoon of this model is shown in Fig. 1. We call this local quasiparticle, with one e_g electron shared over two Mn sites, a dimeron and argue that

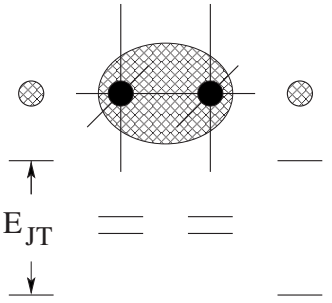

FIG. 1. A cartoon model of the dimeron; the Mn sites are indicated by black solid circles; and O atoms not shown. The shaded oval represents one electron that is shared between the middle two Mn sites. The Mn-O bond lengths (solid lines) on each of these sites are not quite equal; however the distortions on these two sites are comparable such that the small JT splitting of the e_g levels (depicted below) are the same. In contrast the distortion (not shown) of the Mn-O bonds for the two neighboring Mn atoms (left and right), which each have one e_g electron, are larger and lead to large JT splittings of the e_g levels. Because of the significant difference in JT energies, there is a large barrier for an electron in the lowest e_g level on the left or right Mn sites, to hop onto the middle (dimeron) sites.

once established it would be fairly stable as the barriers surrounding it are large. However over time scales long compared to phonons, it will move via activated hopping to account for the observed transport.[43–45]

The formation and reformation of the dimeron as it moves through the lattice is a statistical process and at a given instant not all vacant sites may be paired with an electron site in this way. However our data suggest that a large fraction of the holes introduced via Ca doping do form a low distortion polaron. The dimeron is the smallest unit that allows both a rapid back-and-forth hopping, and a greatly reduced local distortion. Note that it is statistically less probable that three sites would be coupled this way but we cannot exclude the possibility that a few polarons cover more than two sites. Also note that the rapid back-and-forth hopping will promote the double exchange FM coupling proposed by Zener[6] and the two spins should be parallel. Thus the dimeron will also have some properties of magnetic polarons.[46,47] To summarize, the dimeron is a low distortion quasiparticle in a sea of highly distorted sites. When one includes the O neighbors about the two Mn sites that determine the local JT distortions, the size of the dimeron quasiparticle is about 8 Å. We discuss other evidence for such quasiparticles in the discussion section.

In the sense that the polarons (dimerons) in LCMO have a low distortion,[20] they are in some ways the opposite of the usual polaron which has a small local distortion in a lattice with no other distortions except thermal phonons. In fact Billinge[48] has referred to the polaron in LCMO as an"anti-polaron" because of this reduced distortion.

II. EXPERIMENTAL DETAILS

Polycrystalline samples of $La_{1-x}Ca_xMnO_3$ were prepared from 99.99% purity (or better) La_2O_3, $CaCO_3$, and MnO_2. La_2O_3 was dried for 16 h at 500 °C prior to use. The starting

materials were weighed and mixed with an agate mortar and pestle for at least 6 min followed by reaction at 1100 °C for 20 h. The samples were then reground for at least 6 min followed by reaction at 1300 °C for 20 h. This step was repeated four times with reaction temperatures of 1350 °C, for the first time, and 1375 °C thereafter. Finally, the samples were reground for 6 min, pressed into pellets, and reacted for 30 h at 1375 °C. Samples with $x=0.30$, 0.40, and 0.45 were cooled at 2 °C/min to room temperature. The $x=0.21$ sample was removed from the furnace at 1200 °C to limit the absorption of oxygen. The average Mn valence was determined by iodometric titration to be 3.214(5), 3.292(5), 3.400(5), and 3.445(5) for $x=0.21$, 0.30, 0.40, and 0.45, respectively. All samples were characterized using powder x-ray diffraction and determined to be single phase.

To make XAFS samples, the pressed pellets were reground, passed through a 400-mesh sieve, and then brushed onto scotch tape which preferentially holds the smaller grains (≤ 5 μm) in a thin layer. Two pieces of tape (double layer) were pressed together to encapsulate the fine powder. Two or three double layers of tape were then stacked together for the EXAFS measurement to obtain an absorption step at the Mn K edge ~ 0.5 for each sample.

EXAFS data were collected at the Mn K edge as a function of temperature (from 4 to $\sim 300-400$ K) and magnetic field (up to $\sim 8-11$ T) for each of four samples ($x=0.21$, 0.3, 0.4, and 0.45). At SSRL ($x=0.21$ and 0.3), we used Si(111) monochromator crystals and a 0.7-mm slit height to obtain an energy resolution of ~ 1.2 eV; the monochromator was detuned 50% to minimize harmonics. For the SSRL magnet the data were limited to $k \leq 12$ Å^{-1} because of Fe contamination in the Be window. At NSLS ($x=0.4$ and 0.45), a Si(111) monochromator with toroidal focusing mirror was used on beamline X19A; the energy resolution was ~ 1.3 eV. Here the detuning was also 50%. Data were collected for both increasing and decreasing magnetic fields—no evidence for hysteresis was observed. Three or four scans were collected at each T (and B field) for each sample. For the B field measurements, the field was aligned parallel to the tape layers such that the demagnetization factor is negligible.

The magnetization was measured using a vibrating sample magnetometer which is an option in a Quantum Design physical-properties-measurement system. Data were acquired in constant magnetic field while sweeping the temperature at less than 1 K/min. Again to minimize the demagnetization factor, the data were collected on long sample rods with the B field parallel to the rod axis.

A. EXAFS background and data-reduction procedures

The EXAFS oscillations above an x-ray absorption edge provide local structure information about the atom investigated—here about Mn. The absorption, μ, for the Mn K edge (after other absorption contributions have been subtracted) is given by[49]

$$\mu(E) = \mu_o(E)[1 + \chi(E)], \tag{1}$$

where μ_o is the embedded atom absorption for Mn and χ describes the oscillations of the absorption above the edge, produced by backscattering of the photoelectron from neighboring atoms. The energy is converted to k space [$k = \sqrt{2m(E-E_o)}/\hbar \sim 0.512\sqrt{E-E_o}$; where k is in Å^{-1} and E is in eV], to yield the EXAFS equation for $k\chi(k)$ given by

$$k\chi(k) = \sum_i k\chi_i(k)$$

$$= \mathrm{Im}\sum_i A_i \int_0^\infty F_i(k,r)\frac{g_i(r_{0i},r)e^{i[2kr+2\delta_{c,i}(k)+\delta_{b,i}(k)]}}{r^2}dr$$

$$A_i = N_i S_0^2. \tag{2}$$

Here $g_i(r_{0i},r)$ is the pair-distribution function for neighbors at r_{0i} from the central atom (Mn), $\delta_{c,i}(k)$ and $\delta_{b,i}(k)$ are the central and backscattering phase shifts, and $F_i(k,r)$ is the backscattering amplitude. The coordination number N_i and the amplitude reduction factor, S_0^2, (multielectron effects) are constants—independent of T or B; N_i is taken from the structure and S_0^2 is determined at low T.

The first step in the data reduction is to remove the absorption from other atoms and other edges. This background was removed using a fourth order polynomial fit of the pre-edge region between 6320–6535 eV and constrained for energies above the Mn K edge such that the data followed the Victoreen[50–52] formula. A straight line was fit through the data between 6600–7100 eV to determine the edge step height, which was then used to normalize the data. Above the edge, the embedded atom absorption, μ_o, was approximated by a sum of cubic splines with 5 knots (4 splines) up to $k=12$ Å^{-1} for the 21% and 30% Ca samples, and 6 knots up to k of 14 Å^{-1} for the 40% and 45% Ca samples.

Our fits are carried out in r space—obtained by a Fourier transform of $k\chi(k)$ [FT $k\chi(k)$]. Peaks in the r-space plots correspond to various shells of neighbors. In our fits we will use a Gaussian distribution function (or in some cases a sum of Gaussians) for each shell of neighbors; the distribution width, σ, describes the disorder for that pair distance. An additional parameter, ΔE_0, which describes the difference in edge energy between the value defined for the data (arbitrarily set at the half edge height energy) and the theoretical functions (for which $k=0$ at E_0), is also needed, and determined at low temperatures from an average over six or more scans. It is kept constant in subsequent fits for higher T or applied B field.

B. Magnetization data

A major focus of this paper is to correlate changes in the local structure with the sample magnetization. To do so we need magnetization plots as a function of T for various applied magnetic fields (along the axis of a thin-rod sample). These data are show in Fig. 2 for the four samples. The fields were chosen to be the same as used later in the EXAFS experiments. The main features of these data are: (1) above $B \sim 0.4$ T, the magnetization is saturated for all samples; (2) the transition region spreads out as B increases (becomes a crossover) for a range of temperatures near T_c. This is the range in T for which magnetostriction is observed.

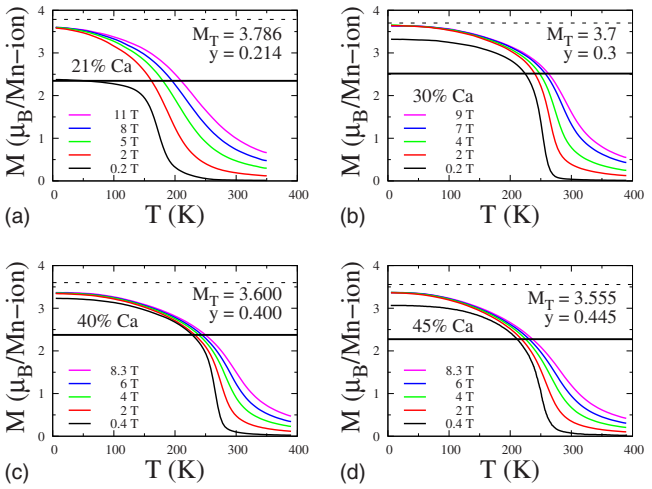

FIG. 2. (Color online) The magnetization as a function of T at several applied B fields, for the four samples (x=0.21,0.30, 0.40, and 0.45). For fields $\geq$2.0 T the magnetization is saturated at low T. The hole concentration y obtained via titration is listed and M_T is the theoretical saturation spin magnetization for the given value of y. The solid horizontal line is the position of the break point discussed in the EXAFS section.

III. TRENDS IN THE EXAFS DATA

Examples of the k-space data, $k\chi(k)$, after the pre-edge and embedded atom backgrounds have been removed and the energy has been converted to k space (see Sec. II A), are shown in Fig. 3(a). The data were then FT to r space using a Tukey window (constant amplitude with Gaussian tails) over a k range of 3.5–11.3 Å^{-1}, with a Gaussian broadening of 0.3 Å^{-1}. The corresponding r-space data for 30% Ca, are shown in Fig. 3(b). In such plots, each peak represents a shell of neighbors about Mn. The first peak at ~1.5 Å corresponds to the nearest O atoms; the next double (overlapping) shell is comprised of Mn-La, Mn-Sr, Mn-Mn, and some multiscattering peaks. As the temperature increases, the r-space amplitude decreases significantly, particularly for the first Mn-O peak where most of the change occurs between 200 and 265K [see Fig. 3(b)]. This amplitude decrease indicates that the disorder of the Mn-O bonds increases (i.e., the width, σ, of the Mn-O PDF increases); the change is largest near T_c. Similar but smaller changes are observed for other atom-pair-distribution functions.

Although some thermal phonon broadening is expected for the MnO_6 octahedra, most of the large disorder of the Mn-O bonds (above T_c) has been attributed to the presence of large Jahn-Teller distortions when a single localized e_g electron is present on many Mn sites. This Jahn-Teller distortion disappears as the sample becomes magnetized (either at lower temperatures or in higher applied magnetic fields) when the electrons hop faster than phonon frequencies and the lattice can no longer respond.

In Fig. 4 we plot the Mn K edge r-space data as a function of B field for the 30% Ca sample for a fixed temperature, 270 K, just above $T_c \sim 262$ K. In contrast to the T dependence, the amplitude of the first peak *increases* in amplitude as B increases. This indicates that the disorder of the Mn-O

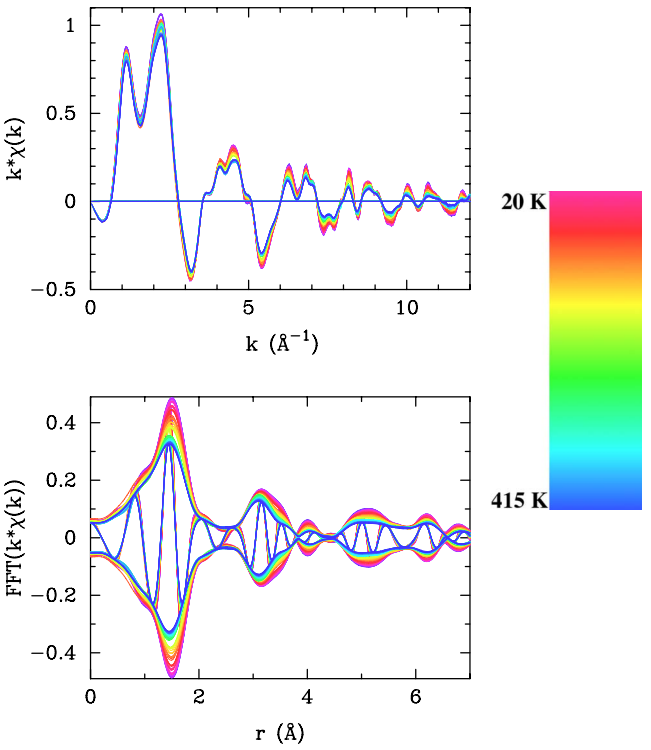

FIG. 3. (Color online) The k-space (top) and r-space (bottom) data for the Mn K edge in $La_{0.70}Ca_{0.30}MnO_3$ as a function of temperature with B=0 T. As the temperature increases, the amplitude of both the k-space and r-space data decreases. In the r-space data (here and in later r-space plots), the fast oscillation is the real part of the Fourier transform (FT_R) while the envelope is $\pm\sqrt{FT_R^2+FT_I^2}$, where FT_I is the imaginary part of the transform. The FT used a k range of 3.5–11.3 Å^{-1} with a Gaussian broadening of 0.3 Å^{-1}.

bonds, and hence the value of σ, has *decreased* as the B field forces more of the sample into the itinerant magnetic phase. Similar results are observed for the other Ca concentrations.

In addition, Fig. 4 also shows a small B-field-induced change near 3.5 Å (the high-r shoulder of the second neighbor peak between 3 and 4 Å) which corresponds to the Mn-Mn pair-distribution function. This provides direct ex-

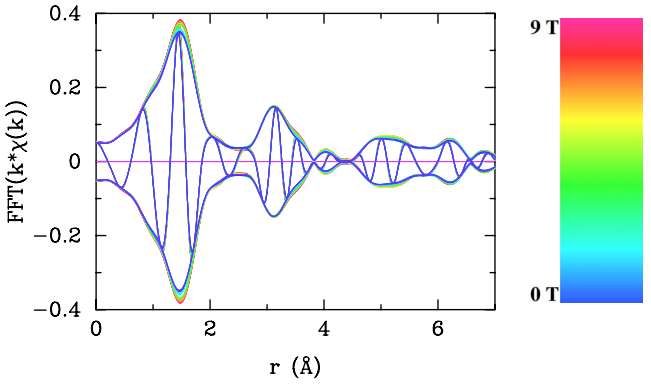

FIG. 4. (Color online) The r-space data as a function of magnetic field B for the Mn K edge in $La_{0.70}Ca_{0.30}MnO_3$ at 270 K, just above T_c(≈262 K).

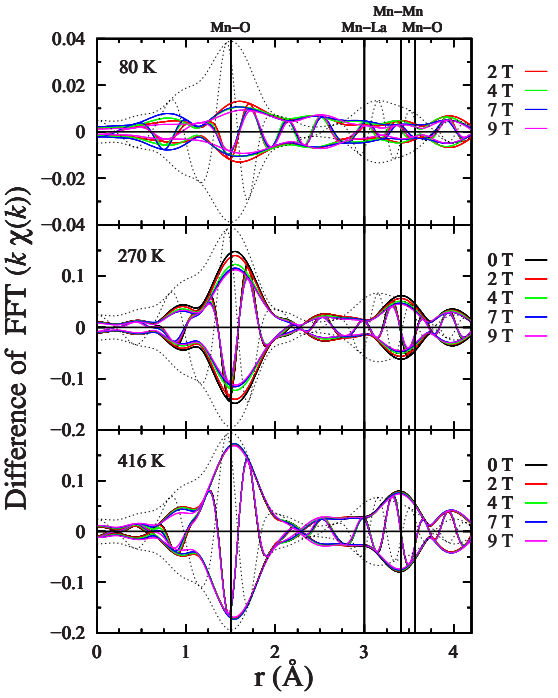

FIG. 5. (Color online) Difference data relative to 20 K, 0 T [i.e., Data (T, B)-Data (20 K, 0 T)] for $La_{0.70}Ca_{0.30}MnO_3$ as a function of applied magnetic field at three different temperatures. Top—80 K (note the smaller vertical scale); middle—270 K (near T_c); and bottom—416 K. The 20 K, 0 T data are shown in the background as a dotted line (rescaled to fit) to provide a reference for where the differences occur relative to the original data. The atom-pair positions are marked by solid vertical lines.

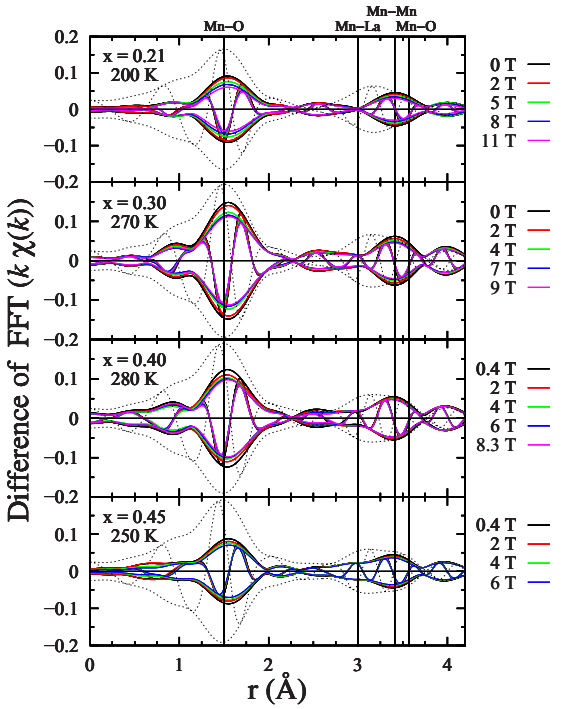

FIG. 6. (Color online) Similar difference data [Data (T, B)-Data (20 K, 0 T)] for T near T_c as a function of field for each of the four samples collected in a magnetic field (x=0.21, 0.30, 0.40, and 0.45). The low temperature, zero-field data (rescaled to fit) are shown as a dotted line to provide a reference for where the differences occur relative to the original data.

perimental evidence for magnetostriction in CMR materials, mentioned in Sec. I. As the magnetic field increases, the Mn-O distortion decreases, shortening the Mn-Mn distance and reducing the lattice constant. In contrast, there is no observed B-field-induced change for the main peak near 3.2 Å which corresponds mainly to the Mn-La pair-distribution function, indicating that the Mn-La pair distribution is unaffected by the applied magnetic field.

The B-field-induced changes can more easily be seen in the difference data plotted in Figs. 5 and 6. Figure 5 shows difference data relative to 20 K, 0 T [i.e., Data (T, B)-Data (20 K, 0 T)] as a function of field for $La_{0.70}Ca_{0.30}MnO_3$ at three different temperatures: low T (80 K), near T_c (270 K), and high T (416 K). The 20 K, 0 T data have been rescaled to fit the vertical axis and are shown as a dotted line to provide a reference for where the differences occur relative to the r-space spectrum. Note that the 80 K data are shown on a smaller vertical scale (factor of 5) and the apparent differences with field are close to the experimental error. Thus, there is no significant difference as a function of B field far away from T_c (at 80 or at 416 K, see Fig. 5). However, there is a large B-field-induced change near T_c for the nearest Mn-O peak near 1.5 Å and a smaller but measurable B-field-induced change for the Mn-Mn peak near 3.4 Å (see Fig. 5: middle). The lack of any significant B-field-induced change for the Mn-La peak near 3.1 Å is very clear in the difference data.

The same type of difference data [Data (T, B)-Data (20 K, 0 T)], but now only for T near T_c, are plotted in Fig. 6 as a function of field for each sample. Each plot shows the same general behavior. There is a large B-field-induced change for the Mn-O and a moderate change for the Mn-Mn peaks with the x=0.3 sample showing the largest overall change.

Details of the fits

To extract detailed structural information from the data, we fit it to a sum of known pair-distribution functions, referred to as "standards;" these are first calculated using FEFF8.[53] We start with a fit to only the Mn-O peak.

Mn-O peak

For the Mn-O distribution, we chose a simplified model of a single Gaussian peak to represent the Mn-O distribution. This provides a single parameter to represent the distortion for comparison with the sample magnetization. In this model, the width (σ) of the Gaussian distribution function is a direct measure of the average distortion of all the Mn-O bonds and provides the ability to directly correlate changes in the distortion (as a function of temperature or magnetic field) with the sample magnetization. Other authors[21,30] have used multiple Mn-O peaks to try to determine further details of the Mn-O distortion but then there is not a single parameter available to compare with magnetization. As we will see in Sec. IV, the first Mn-O peak can indeed be fit with two

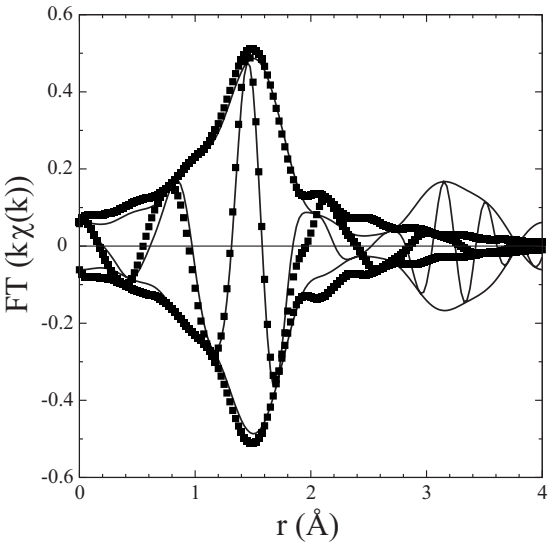

FIG. 7. An example of the fit of the first Mn-O peak using a FEFF theoretical standard for 30% Ca at $T=20$ K and $B\sim 0$ T.

peaks—one at a short distance (≈1.93 Å), representing the undistorted sites when a hole is present and also the short bonds of the distorted sites; and a second peak at a longer distance (≈2.07 Å), representing the long bonds of the distorted sites. Then, by applying a series of constraints to keep the parameters within physical limits, the fraction of long bonds, extracted as a function of temperature or magnetic field can be used as the single parameter needed to correlate with magnetization. The results of both fitting models produce similar results.

The initial results published in Ref. 24 used a single Mn-O standard function calculated with FEFF6—a sum of three peaks with slightly different bond lengths, using the structure of $La_{0.667}Ca_{0.333}MnO_3$ given by diffraction.[54] The amplitude of the Mn-O peak ($A=NS_0^2$) was constrained to 4.2 (similar to earlier studies[20,22,38,55]), where $N=6$ for the nearest oxygen neighbor and $S_0^2=0.7$. ΔE_0 was constrained to the value at low temperature and only the r shift and σ were allowed to vary.

However, this fitting model had a minor inconsistency. Although it has no significant effect on the earlier results, it led us to improve the fitting model for the more recent high field data (the earlier data for 21 and 30% were also refit using the new model for consistency). The main problem was that at the lowest temperatures, σ was consistently a bit too small, i.e., σ^2 at 4K was slightly below the value for the zero-point motion of the correlated Debye model, an unphysical result. This arose in part because the Mn-O standard described above was constructed from the sum of three different Mn-O standards at slightly different pair distances and the standard itself had a small width from this distribution. Consequently, the σ parameter extracted from the fit represented only the *excess* width above the inherent width in the standard. At this point, it is important to note that the absolute error for σ depends on (1) the error in S_0^2 and (2) on the FEFF calculation (both constant systematic errors), which together may be on the order of 10%. These systematic errors primarily change the static component of σ and shift the plot

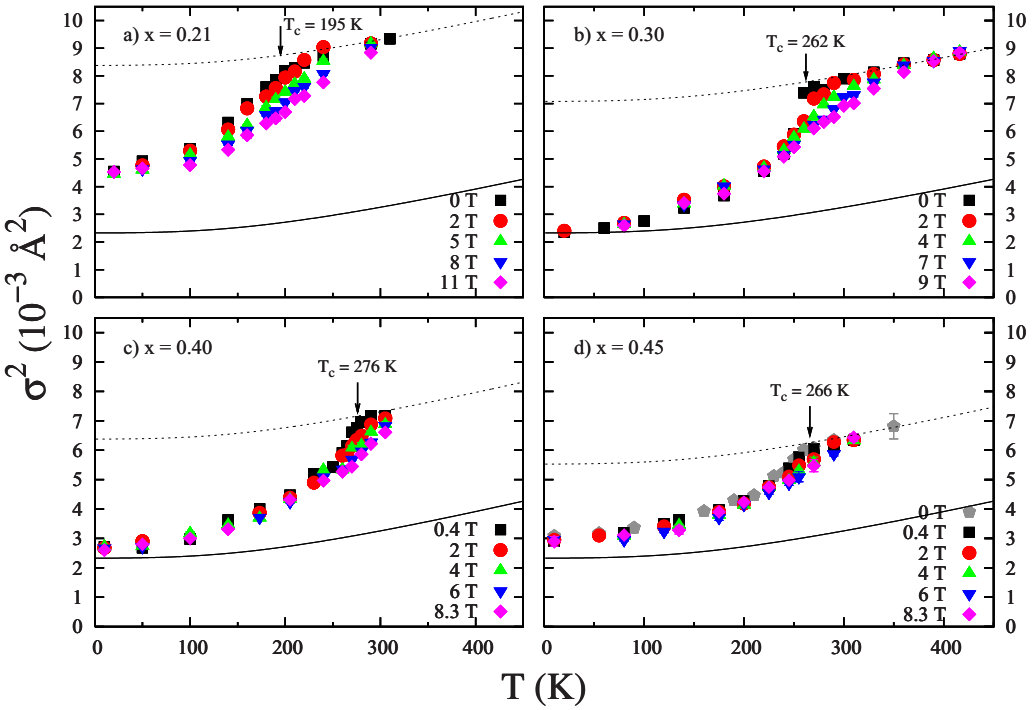

FIG. 8. (Color online) σ^2 for the Mn-O PDF, as a function of temperature and applied magnetic field for four samples. The solid line is a fit of $\sigma^2(T)$ for the Mn-O peak in $CaMnO_3$ to a correlated Debye model with $\theta_D=860$ K, and represents the contribution to σ^2 from thermal phonons. $\sigma^2(B,T)$ increases rapidly just below T_c (indicated by an arrow), which is attributed to the increase of JT distortions as the temperature is increased into the paramagnetic insulator phase. The dashed line is the thermal phonon contribution plus a large static offset corresponding to the maximum JT and polaron distortion plus possibly a small static contribution.

of σ^2 vs T vertically. For this reason, we were not concerned about the small negative static offset required to fit the low-temperature data points to the correlated Debye model for Mn-O; we focused instead on the *change* in σ^2 as a function of temperature or magnetic field.

To eliminate this problem, a new Mn-O standard function was calculated using the newer version of FEFF–FEFF8 (Ref. 53) and the structure of the end compound, $CaMnO_3$, where the three Mn-O distances are within 0.02 Å of each other. Further we used only the middle peak function so that there is no intrinsic broadening in the standard. This standard, however, would require a large r shift to fit the Mn-O data since the $CaMnO_3$ unit cell is much smaller than that of the doped samples. Therefore, in the new fitting model, the Mn-O standard function was calculated from the structure of $CaMnO_3$ (given in Ref. 15) but with the lattice constants multiplied by 1.026 to enlarge the unit cell to be comparable to that of $La_{1-x}Ca_xMnO_3$; this effectively shifted the middle Mn-O distance to ~1.95 Å which is close to the average Mn-O distance in the doped samples studied here. With this standard, the average value of $S_0^2=0.79$ for several low-temperature scans and thus the amplitude of the Mn-O peak was constrained to 4.75 (≈13% larger than the previous value). This value of A gave σ^2 values consistent with the zero-point motion of the correlated Debye model for $La_{0.70}Ca_{0.30}MnO_3$ but did not change the T dependence significantly. The other four samples were constrained to the same amplitude such that any excess distortion remaining at low temperature could be compared across the concentration range. Again, ΔE_o was constrained to the value at low temperature (≈9.7 eV for $La_{0.70}Ca_{0.30}MnO_3$), and only the r shift and σ were allowed to vary. An example of a fit to the first neighbor Mn-O peak is shown in Fig. 7 for the 30% Ca sample at $B=0$ T and $T=4$ K.

From these fits we extract $\sigma(B,T)$ for the Mn-O peak over a wide range of parameter space for the four concentrations $x=0.21$, 0.3, 0.4, and 0.45. This provides a single parameter, σ^2, to characterize the average distortion of the Mn-O bonds throughout the sample, and allows a simple correlation with the sample magnetization to provide insight as to how the distortions change as the sample passes through the ferromagnetic transition.

Note that when various broadening mechanisms are uncorrelated their contributions add in quadrature

$$\sigma^2_{total}(B,T) = \sigma^2_{phonon}(T) + \sigma^2_{static} + \sigma^2_{\mathrm{JT}/polaron}(B,T). \quad (3)$$

For example, if δr_{phonon} is the change in bond length from phonons and δr_{JT} is the change (same bond) from a JT distortion, then the time average—$\langle \delta r_{phonon} \delta r_{\mathrm{JT}} \rangle$ is zero, when these displacements are uncorrelated.

When only phonons produce fluctuating variations in bond lengths, the temperature dependence of σ^2 can be accurately described by a correlated Debye model given by Eq. (4) [this models σ^2(T) for the Mn-O bond in $CaMnO_3$ very well]

$$\sigma^2_{cDebye}(T) = \frac{3\hbar}{2m_r}\int_0^{\omega_{cD}} \frac{\omega}{\omega^3_{cD}} C_{ij} \coth\left(\frac{\hbar\omega}{2k_BT}\right) d\omega, \quad (4)$$

where C_{ij} is the correlation function $[1-\sin(\omega r_{ij}/c)/(\omega r_{ij}/c)$; $c=\frac{\omega_{cD}}{k_D}]$ where k_D is the Debye wavenumber, m_r is the reduced mass, and ω_{cD} is the correlated Debye frequency. If no static disorder is present, σ^2(4 K) corresponds to the value for zero-point motion.

In Fig. 8 we plot $\sigma^2(B,T)$ of the Mn-O PDF as a function of temperature and B field for the four samples. All the data were fit to the new standard (with $S_0^2=0.79$), as described above, so that disorder between samples can be compared. For the older data (21% and 30% Ca, presented in Ref. 24) the σ^2 results here are shifted slightly vertically, compared to the earlier report. For a given sample at low T or well above T_c, the data for different values of B field all collapse onto the same line. However for a range of temperatures near T_c the curves are spread out, consistent with the B field dependence of the r-space data shown in Fig. 6. This is the same regime for which magnetostriction is observed.[31–37]

For these samples as well as other compositions[25] we find that the T dependence above T_c is the same as that for undistorted $CaMnO_3$. Consequently we can easily remove the thermal phonon contribution by subtracting the contribution for $CaMnO_3$ (solid lines in Fig. 8) to obtain $\sigma^2_{\mathrm{JT}/polaron} + \sigma^2_{static}$, as shown in Fig. 9 (lower panel) for the 30% sample at two fields 0 and 9 T. Then above T_c the data are flat—independent of T (see similar plots for lower concentrations in Ref. 25). This indicates that the nonphonon distortions above T_c are constant. In particular, there is no change over the temperature range just above T_c where polaron correlations show a peak in neutron-diffuse scattering;[56,57] although these correlations show up in neutron scattering there is no significant decrease in the distortions around the polarons until significant FM clusters are formed. Note that the small T-independent structure (~1 nm in size) observed in the neutron data above T_c, that is associated with polarons,[56,57] is

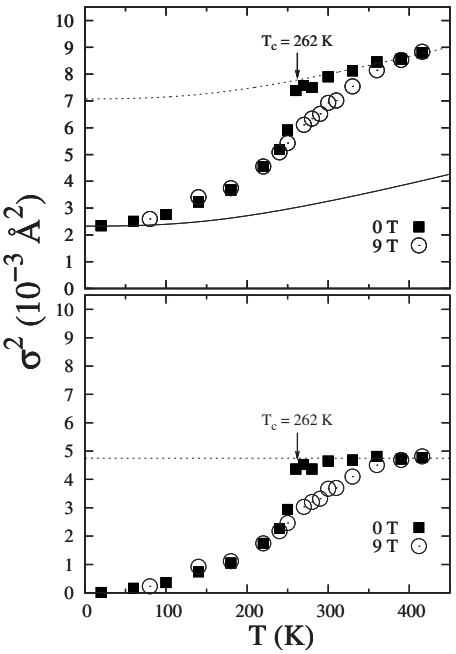

FIG. 9. (Upper panel) $\sigma^2(T)$ as a function of T for $B=0$ and 9 T. (Lower panel) The remaining contribution ($\sigma^2_{\mathrm{JT}/polaron}+\sigma^2_{static}$) after the phonon contribution (solid line—from $CaMnO_3$) has been subtracted for the data in top plot; for this sample, $\sigma^2_{static} \sim 0$. In particular, note that at high T the plot is flat, independent of T.

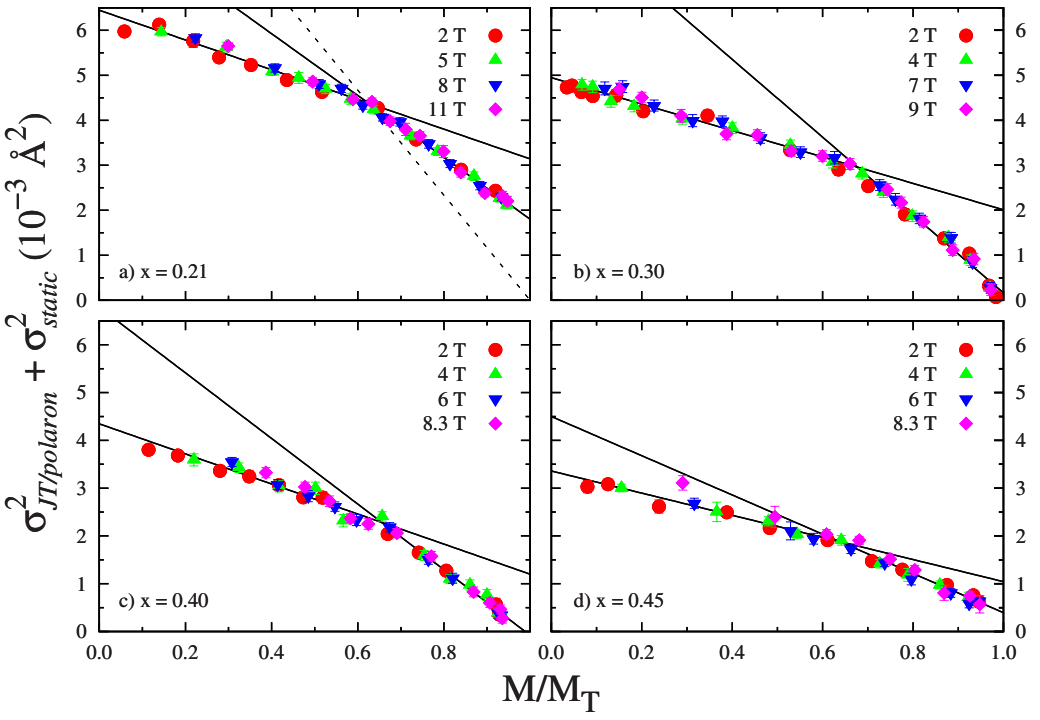

FIG. 10. (Color online) The average distortion per site due to the presence of JT distortions and polarons–$\sigma^2_{\mathrm{JT}/polaron}$ (plus any temperature-independent static distortion σ^2_{static}) versus the fraction of magnetized sites (M/M_T), where M_T is the theoretical maximum magnetization given by the hole concentration—see Fig. 2). For each sample, there is a low initial slope until the sample is ~60–70% magnetized; then the slope (i.e., the distortion removed per magnetized site) increases. For the 21% sample, some JT distortion remains at low T, even at high B field. To include this sample in a comparison of the high slopes, note that the high slopes for other samples correspond to the full removal of the JT distortion as M approaches M_T. Consequently, for 21%, we draw the dotted line through the break point, to $\sigma^2_{\mathrm{JT}/polaron}=0$ at $M/M_T=1.0$. See text.

consistent with the lack of change in $\sigma^2_{\mathrm{JT}/polaron}$ above T_c.

In addition, the positions of the Ca ions must constrain how the magnetization develops, because for charge neutrality,[24,42,58] the holes cannot be too far away from Ca sites. Therefore, if the magnetic clusters for $M/M_T<0.6$ are formed from dimeron aggregation, as proposed, then there will be filaments of undistorted magnetized regions (which connect unit cells containing Ca ions) interspersed with filaments of the excess JT-distorted, insulating regions. The development of the magnetization in this way leads to filamentary conducting, magnetic clusters separated by insulating, nonmagnetic regions.

The notation JT/polaron implies that there are at least two types of distortion: (1) JT distortions about Mn^{+3} sites far from Ca dopants and (2) distortions about the polarons which may be different (plus essentially undistorted Mn sites in the FM phase). For the 30% sample, $\sigma^2_{\mathrm{JT}/polaron}$ goes to zero at low T and σ^2_{static} is negligible, but for 21%, a significant σ^2 value remains at 4 K (after subtracting the thermal contribution), which we attribute primarily to some remaining JT distortion. There might also be some small, temperature-independent, static contribution but our results are consistent with this contribution being negligible for all samples; however we include the σ^2_{static} term in the y label. We estimate that any static contribution is less than 0.5×10^{-3} Å^2.

To explore the correlation between JT/polaron distortions and the sample magnetization, we plot in Fig. 10, $\sigma^2_{\mathrm{JT}/polaron}$ (from Figs. 8 and 9) vs M/M_T (using the magnetization data in Fig. 2). In this plot both T and B are hidden variables. Here one can clearly see that the total distortion per site, that arises from the JT interaction, is high when the magnetization is low, i.e., at high temperatures. As the sample becomes magnetized (either by lowering the temperature or by applying an external magnetic field), the average distortion per site begins to decrease, slowly at first, until the sample is approximately ~60–70% magnetized (i.e., $M/M_T\approx0.6$–0.7). At still lower T (or higher B) the average distortion per site (σ^2) decreases faster as the fraction of magnetized sites (M/M_T) approaches 100%. Note that on this plot the left side is for high temperature (low M) while the right side is low T (high M).

In contrast to the limited earlier study of the B-field dependence (for 21% and 30% Ca),[24] we also exclude all the low B-field data and only plot results for $B\geq2$ T. Then within our errors, we observe *complete universality* for each sample. $\sigma^2_{\mathrm{JT}/polaron}$ only depends on the magnetization and is independent on how the magnetization is achieved, via a change in temperature, a change in magnetic field B, or both. Thus the dependence shown for each sample in Fig. 10 becomes a calibration plot between $\sigma^2_{\mathrm{JT}/polaron}$ and the fractional magnetization.

The plots in Fig. 10 are well described by two straight lines with a break point near $M/M_T\sim0.65$. With the additional high field data for the $x=0.4$ and 0.45 samples, it has become clear that this crossover point is not a function of hole concentration, as previously thought.[24] For low B fields

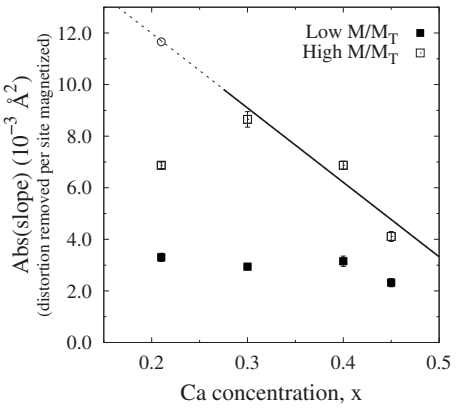

FIG. 11. The magnitude of the slopes of the best fit lines for the plot of $\sigma^2_{JT/polaron}$ vs $M/M_T(T)$ (Fig. 10) as a function of Ca concentration. The low slope (solid squares) is essentially independent of x while the high slope (open squares) decreases roughly linearly with x, for $0.3 \leq x \leq 0.45$—see solid line. When we use the dashed line in Fig. 10 for the 21% Ca sample, (open circle) the dotted line extension of the solid line goes through the circle. If we use the solid line in Fig. 10 for the 21% sample—which leaves a large distortion present at low T then the high-slope is smaller (open square).

we have found that the breakpoint is not as well defined and more importantly, its position varies with B field. Only for high fields does it become essentially independent of B field. For $M/M_T < \sim 0.65$ (i.e., a small T range just below T_c) the distortion removed per magnetized Mn site is small—i.e., the (negative) slope of this line is small. Furthermore this slope is the same for all samples, suggesting a similar, small local distortion for a large fraction of Mn sites. We associate these small-distortion Mn sites with the polarons—note that the polarons must involve both hole and electron sites; also a static hole site would have very little distortion. When the holes are hopping and the double exchange interaction is operative, each hole is hopping between at least two sites so the fraction of low distortion sites will be larger than the hole concentration.

For large magnetization ($M/M_T > \sim 0.65$), the decrease of $\sigma^2_{JT/polaron}$ with M is much faster, indicating that a large distortion per site is removed as these Mn atoms become magnetized. In addition, the slope of this line is concentration dependent and decreases in magnitude with increasing Ca concentration. The concentration dependence of these two slopes is shown in Fig. 11. Note that Bozin *et al.*[30] also reported a decreasing JT distortion as the Ca concentration increased.

For the 21% sample, a significant JT distortion remains at low T, even though most of the sample is magnetized above $B=2$ T. Such a large remaining distortion on some sites, inhibits the rapid hopping that is needed for a DE magnetic coupling, and likely another mechanism (a ferromagnetic superexchange or proximity effect) plays a role at lower concentrations for these distorted sites. Consequently to compare with the other samples for which JT distortions are ~0 at 4K, and hence the DE mechanism dominates in the magnetic coupling (the DE exchange mechanism is maximized when distortions are zero), we draw a straight line through the break point to the point for which $\sigma^2_{JT/polaron}=0$ at $M/M_T=1$ (dashed line in Fig. 10), and plot this slope as a circle for the 21% sample in Fig. 11. Note that when we do so, the circle lines up nicely with the straight line through the points for the higher Ca concentrations. Then, the high slope decreases nearly linearly with x and appears to be the same as the low slope when x approaches $x=0.5$. This is suggestive that the low slope corresponds to a pair of Mn sites. It also suggests that the orbitally ordered regime observed for 50% doping might be viewed as an ordered arrangement of AFM coupled dimerons.

The data clearly indicate that there are two quite different distortions of the Mn-O bonds in the CMR manganites for unmagnetized sites and very little JT distortion (and hence a negligible JT splitting energy) for the magnetized sites.

When large JT distortions are present, it costs significant energy for an electron to hop from a highly distorted site to a nearly undistorted (possibly magnetized) site; thus energetically, the low distortion sites (with the smallest E_{JT}) will magnetize first. Consequently only after most of the holes are incorporated into the magnetized phase do the sites with large distortions begin to become magnetized. We discuss possible models in the discussion section.

In Fig. 10 we have shown that the JT/polaron distortion is a universal function of magnetization if the sample is sufficiently magnetized, i.e., for applied fields ≥ 2 T. However, at low B fields (≤ 0.4 T) the data do not follow the same relationship and this deviation grows as the field decreases toward zero. On plots similar to those in Fig. 10 the low field results fall below the straight lines. This suggests that the fraction of magnetized sites is actually larger than inferred from the bulk magnetization, i.e., small clusters of locally magnetized Mn sites with a reduced distortion, must exist, but they may be canted relative to each other and/or to the applied magnetic field, such that the overall sample magnetization is smaller than expected. Furthermore, for the 21% Ca sample at $B=0.2$ T, the apparent fraction of magnetized sites seems to saturate at $M/M_T \sim 0.60$ from the bulk magnetization data, but the average distortion from EXAFS continues to decrease as T is lowered. Even when the EXAFS data and the magnetization data were both collected in the same small applied magnetic field $B=0.4$ T (i.e., for the 40% and 45% data), the bulk magnetization is still slightly smaller than expected.

Instead of plotting these low B-field results in the same way as shown in Fig. 10, we present them from a different perspective, that provides additional insight. We assume that the universal relationship between the local structure and the fraction of magnetized sites that was found for the higher applied magnetic fields (see Fig. 10), holds for all fields. Then from $\sigma^2_{JT/polaron}$ we can estimate the fraction of locally magnetized Mn sites; note that $\sigma^2_{JT/polaron}$ is independent of any canting of the Mn spins. Figure 12 compares the bulk magnetization (y axis) (see Fig. 2) with the local fraction of magnetized sites (x axis) obtained from the measured value of $\sigma^2_{JT/polaron}$ (and the conversion from $\sigma^2_{JT/polaron}$ to M/M_T using the plots in Fig. 10). If the local magnetization were the same as the bulk magnetization, the data would all lie on the dotted line as occurs for the high field data. However, for all samples, the EXAFS data measured at low magnetic

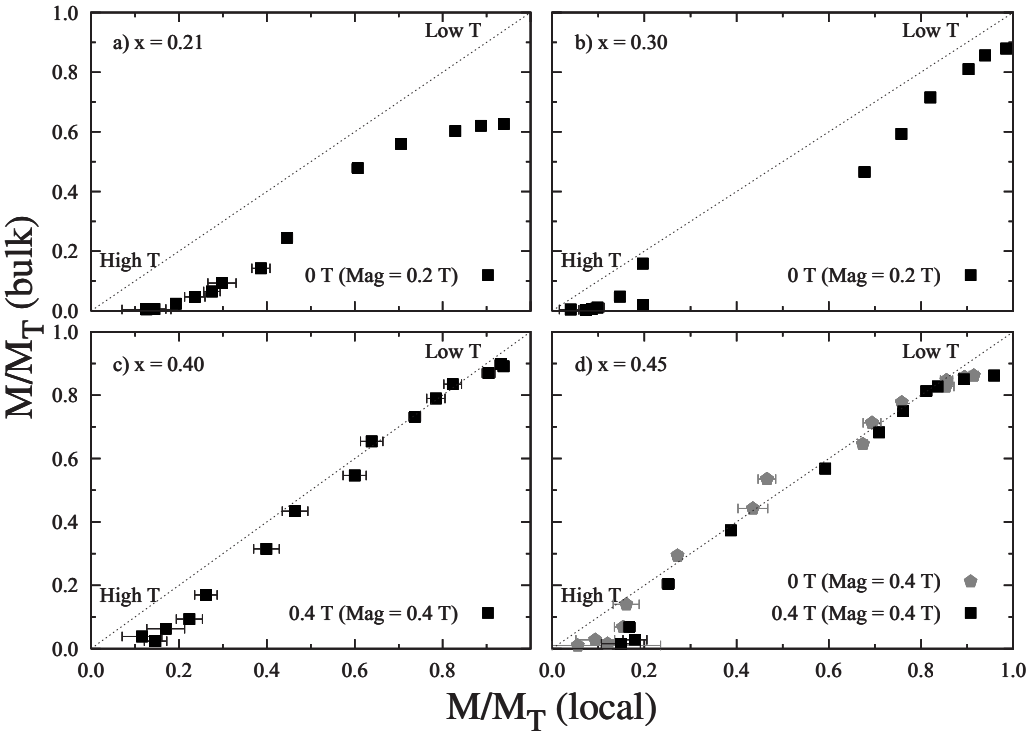

FIG. 12. The bulk magnetization, obtained using a vibrating sample magnetometer (see Fig. 2), versus the local magnetization inferred from the amount of distortion measured from the EXAFS data (using the plots in Fig. 10). The field in which the EXAFS data were measured is given in the label, with the field in which the magnetization was measured, given in parentheses.

fields show that the fraction of locally magnetized sites is actually higher than determined from the bulk magnetization, i.e., the data lie to the right and below the dotted line in Fig. 12. The difference is largest for the 21% and 30% samples where the magnetization is not fully saturated at even 5 K for 0.2 T (see Fig. 2). For the two samples measured at 0.4 T (40% and 45%), the local magnetization (from $\sigma^2_{\mathrm{JT}/polaron}$) agrees reasonably well with the bulk magnetization at low temperatures but as the temperature is increased [i.e., $M/M_T(T)$ is reduced], they begin to deviate. The bulk magnetization underestimates the fraction of magnetized sites, most likely due to a few small ferromagnetic domains that are canted relative to each other at low B fields (thus reducing the overall sample magnetization).

IV. EXPERIMENTAL STANDARDS AND FURTHER NEIGHBOR FITS

As mentioned earlier, the standards used to fit the data, can be either theoretically calculated (FEFF) or experimentally determined. For one-peak fits the difference in the temperature dependence between theoretical and experimental standards is usually very small. If however, a peak is split sufficiently that two peaks can be resolved, then it may be important to carry out a two-peak fit, particularly for comparisons with other works.[21,30] Then the quality of the EXAFS standard becomes crucial as errors in a standard function may show up as a weak nonphysical peak[59] or interfere with another weak peak such that the parameters for the weak peak are not correct. In a two-peak fit there are strong correlations between the splitting δr of the two peaks and the σ's for the two peaks. One can in fact show[60] that if there are N_1 bonds in the first peak and N_2 bonds in the second ($N_1+N_2=6$ for the Mn-O bonds) then

$$\sigma^2_{onepeak} = \frac{1}{6}\{N_1[(r_1 - r_{av})^2 + \sigma_1^2] + N_2[(r_2 - r_{av})^2 + \sigma_2^2]\}, \tag{5}$$

where r_1, r_2, and r_{av} are the bond lengths for the two peaks and their average, and σ_1 and σ_2 are the corresponding widths. This shows explicitly that for a fixed value of $\sigma^2_{onepeak}$ from a one-peak fit, there are a range of values possible for σ_1^2, σ_2^2, and the splittings $(r_i - r_{av})^2$.

In this section, we present fits of the first shell Mn-O pair distribution using two experimental standards to minimize the problems discussed above. First an experimental standard for Mn-O was extracted from pure $CaMnO_3$ for which the six Mn-O bond lengths are very nearly the same; we followed the same procedures as in the past.[59] Briefly, we fit the data for $CaMnO_3$ out to ~4 Å and then subtracted the further neighbor results from the original data to leave the Mn-O peak in r space. Then this peak was back Fourier transformed to provide a k-space standard. The FT ranges and fit ranges were slightly longer than will be used in fitting the LCMO data. Figure 13 shows a comparison in r space of this Mn-O experimental standard with a theoretical standard calculated from FEFF. Although the two standards agree quite well through the main portion of the peak, they clearly deviate on the high-r side of the peak near ~1.9–2.2 Å.

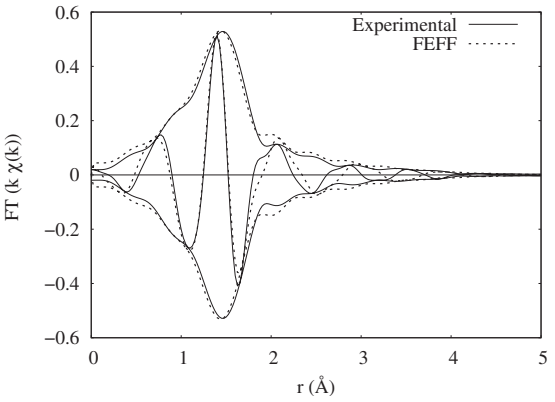

FIG. 13. Comparison of the experimental Mn-O standard derived from $CaMnO_3$ (solid line) and the Mn-O standard calculated from FEFF (dashed line). The two standards deviate on the high-r side of the peak (near 1.9 Å), where the experimental standard does a better job of fitting the low T data; cf. Fig. 14, for which there is a single Mn-O peak at 20 K.

A similar high-r deviation between a FEFF standard and an experimental standard is found for every experimental standard that we have extracted[59] for a number of simple compounds—the FEFF standard is always a bit higher on the high-r side of the peak. Improving the standard on the high-r side of the Mn-O peak is crucial when trying to fit with two peaks since the longer bond peak corresponds to only a few neighbors and is usually quite small. Note that the agreement below ~1 Å, is not important as errors in the background removal show up at low r and fits generally do not go include the low r range.

Kurczveil[61] has recently shown for two samples (30% and 40% Ca samples), that a very similar relationship between the local structure and magnetization exists if the fraction of long Mn-O bonds is used to represent the average amount of JT/polaron distortion, instead of the broadening of a single Mn-O Gaussian distribution. The fraction of long bonds is determined from the relative amplitude of the longer Mn-O standard in the two-peak fit of the nearest-neighbor Mn-O distribution. However, to obtain a robust result for the nearest-neighbor structure using a two-peak fit for the Mn-O distribution, some further neighbor pair-distribution functions (e.g., Mn-La/Ca and Mn-Mn) also need to be included, due to the non-negligible contribution from the tails of these peaks, over the r range of the Mn-O peak. Kurczveil[61] used an approximate fit of the further neighbors. Here we include a full fit out to 4.25 Å, as a function of T and B for each sample; we used six theoretically calculated standards (using FEFF8) to represent the Mn-Ca ($8x$ neighbors), Mn-La [$8(1-x)$ neighbors], Mn-Mn (six neighbors), and two sets of further neighbor Mn-O (12 neighbors) single scattering paths—plus a standard for the 36 Mn-O-Mn multiple-scattering paths.

For the two Mn-O peaks, five parameters are required if there are no constraints:—two r_i, two σ_i, and the fraction of long to short bonds. To reduce this number, the width of the short Mn-O first neighbor was first constrained to follow the correlated Debye model with a Debye temperature (θ_D) of 860 K (calculated from a fit of the width of the Mn-O distribution in $CaMnO_3$) as a function of temperature. Preliminary fits using these four parameters for the Mn-O distribution showed that the position of the long Mn-O bond did not change much (approximately 2.065 ± 0.02 Å) for all samples; consequently in subsequent fits, to reduce the scatter in the parameters σ_2 and $N_2/6$, the length of the long Mn-O bond was constrained to 2.065 Å. Only the short Mn-O bond length, the width of the long Mn-O PDF, and the ratio of the amplitudes were allowed to vary. When using the experimental Mn-O standards, no ΔE_0 or S_0^2 parameters are needed; the amplitudes for these two peaks will be given as fractions ($N_1/6$ and $N_2/6$).

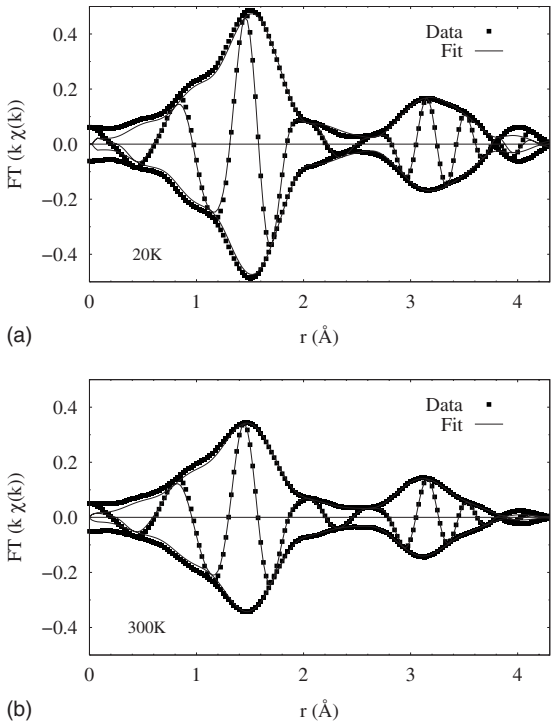

FIG. 14. The fit results for $La_{0.70}Ca_{0.30}MnO_3$ at (a) $T=20$ and (b) 300 K ($B=0$ T), using two experimental standards for the first Mn-O neighbor and six theoretical standards for the further neighbors. The data are shown as solid square points while the fit is shown by solid lines. The FT range was 3.5–11.3 $Å^{-1}$, and the fit range was 1.2–4.25 Å.

For the further neighbors, S_0^2 and ΔE_0 were constrained to the values determined from the fit of the first Mn-O neighbor to a single theoretical standard (i.e., $S_0^2=0.79$, and $\Delta E_0 \approx 9.8 \pm 0.2$ eV, see Sec. IIIA) for each sample. The amplitude for each peak was constrained to the number of neighbors for that peak, multiplied by S_0^2. The width of the Mn-O-Mn multiple-scattering distribution was constrained to be the same as the width of the Mn-Mn distribution, since to first order, the multiple-scattering path length is determined by the distance between the end points (namely, the Mn-Mn distance). In addition, the r shift of the Mn-O-Mn multiple-scattering was constrained to be the same as the Mn-Mn r shift and the r shifts of the two sets of Mn-O second neighbors were constrained such that the overall size of the unit cell can grow or shrink uniformly. The r shift and width of the Mn-Ca and Mn-La distributions, as well as the width of

the Mn-Mn and both Mn-O second neighbor distributions were allowed to vary. In total, 11–12 parameters were allowed to vary, significantly less than the maximum number from Stern's criteria.[62] Fig. 14 shows examples of the fit result for $La_{0.70}Ca_{0.30}MnO_3$ at $T=20$ and 300 K, for $B=0$ T. The data are shown as points and the fit results are shown as a solid line. The fits agree with the data up to ~4 Å. The last peak (the Mn-O second neighbor), does not fit as well because the contributions from the further neighbor peaks are not included. Note that the fit agreement for the first Mn-O peak in Fig. 14(a) at 20 K, which is essentially a one-peak fit to the Mn-O distribution (the amplitude of the long Mn-O peak is ~0 at low T for 30% Ca), is better than using the theoretical FEFF function in Fig. 7. From these fits we extracted the fractions of long and short Mn-O bonds for the two-peak fit model.

In Fig. 15, the relative fractions of both the short (top) and long (bottom) Mn-O bonds are plotted as a function of temperature and magnetic field. At low temperature the nearest-neighbor Mn-O peak consists primarily of short Mn-O bonds. As T is increased up to T_c, Jahn-Teller distortions develop and the fraction of long bonds increases to ~20–40%. In addition, when a magnetic field is applied near T_c the relative fraction of long bonds decreases as the field increases and the JT distortion is reduced. For the 21% sample however, there is still a significant fraction of long bonds present (i.e., ~20%) in the nearest neighbor Mn-O PDF at low temperature. As suggested previously (see Fig. 10), this is likely the result of a few regions of JT distorted Mn sites that remain at low T when the sample is well into the ferromagnetic state. In comparing the two results, the fraction of long Mn-O bonds in the two Mn-O peak fit is roughly equivalent to the increased width of the Gaussian distribution in the one Mn-O peak fit, representing the average JT distortion of the nearest-neighbor Mn-O structure. An expanded view of the fraction of long Mn-O bonds (lower portion of Fig. 15) is shown in Fig. 16, where the change with field near T_c can be seen more clearly. Note that for low B fields the changes are rapid just below T_c and then the amplitude becomes essentially constant above T_c. The amplitudes are independent of B at 4K and well above T_c but have a large variation with B near T_c—over the same range as the observed changes in $\sigma^2_{JT/polaron}$ in Fig. 9 (bottom).

Using the fraction of long bonds to represent the local Mn-O distortion, we obtain the relationship shown in Fig. 17, between the Mn-O distortion and magnetization. Again a universal relationship is found when $B \geq 2$ T—compare Fig. 17 with Fig. 10. Not only is there universal behavior for a range of B fields and temperatures but the plot again is described by two straight lines and the low slope line has nearly the same slope for each sample.

As T increases from ~4 K, not only does the fraction of long bonds increase as the JT distortions develop but the average position of the short Mn-O bond also decreases. This can easily be seen in Fig. 18, where the length of the short Mn-O bond is plotted as a function of temperature and magnetic field for each sample. At low temperature, the average position is ~1.94–1.96 Å, depending on the sample. As the temperature is increased up to T_c, the average position of the short Mn-O bond decreases to ~1.93 Å, as long bonds near ~2.07 Å develop. In the transition region where both JT-distorted and magnetic regions coexist, the short bondlength will be an average of the short bonds on JT-distorted sites and the bond length in the magnetic phase—for the 30% Ca sample for example, a weighted average of ~1.93 and ~1.96 Å bond lengths. Consequently, when a magnetic field

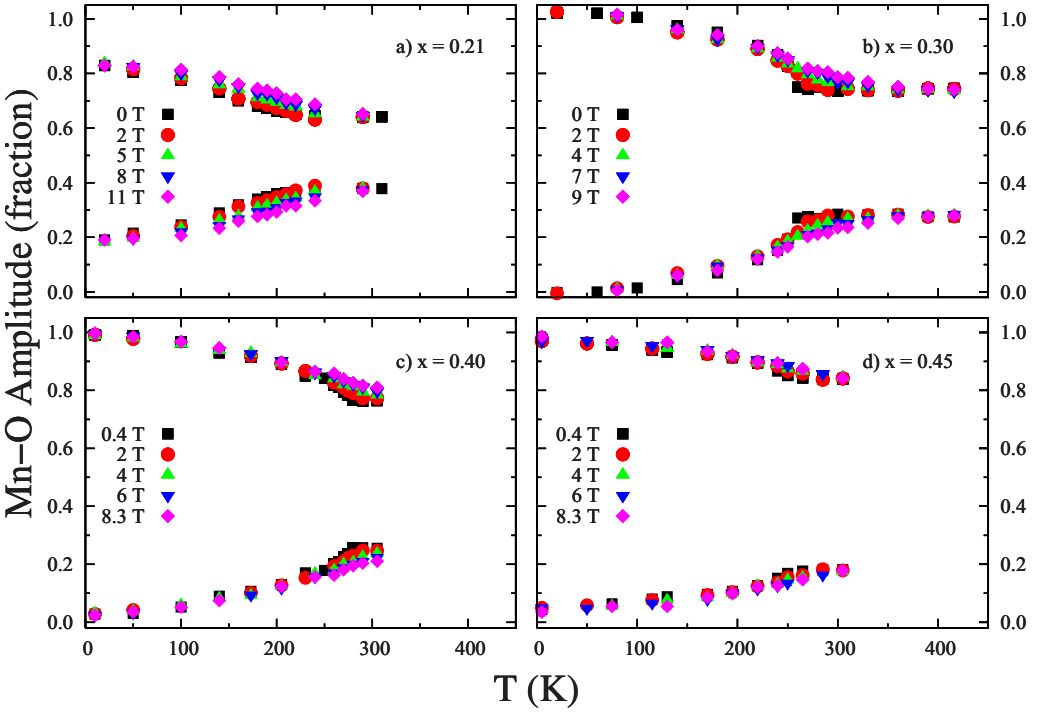

FIG. 15. (Color online) Relative fraction of the short (~1.93 Å) Mn-O bonds (top) and the long (~2.07 Å) Mn-O bonds (bottom) as a function of temperature and magnetic field for each sample.

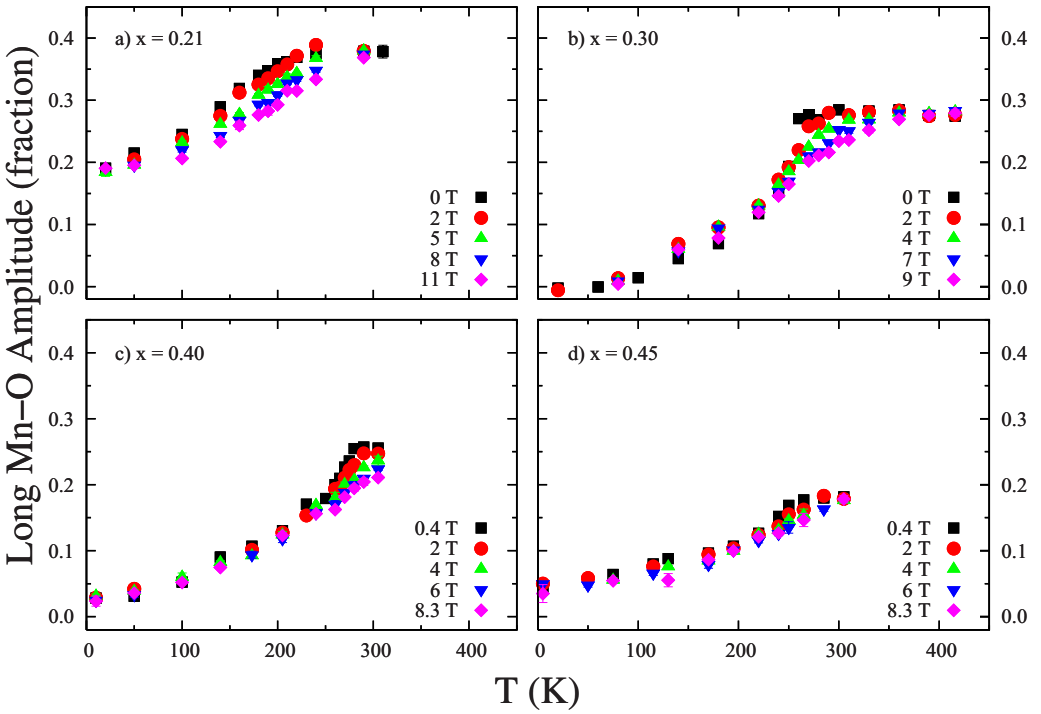

FIG. 16. (Color online) An Expanded view of the fraction of long Mn-O bonds (at ~2.07 Å, i.e., the lower portion of Fig. 15) as a function of temperature and magnetic field for each sample.

is applied just below T_c, the average position of the short Mn-O bond will shift to a slightly longer distance with increasing B field as the magnetized fraction increases. Note that EXAFS is more sensitive to shorter bonds from the $1/r^2$ dependence in the EXAFS equation [see Eq. (2)]. Consequently, because in the two-peak fit a fraction of the amplitude is already been accounted for by the long bond at ~2.07 Å, this splitting of the Mn-O PDF enhances the shortest bond length as reported previously in Ref. 20 as a function of temperature. However, the detailed changes as a

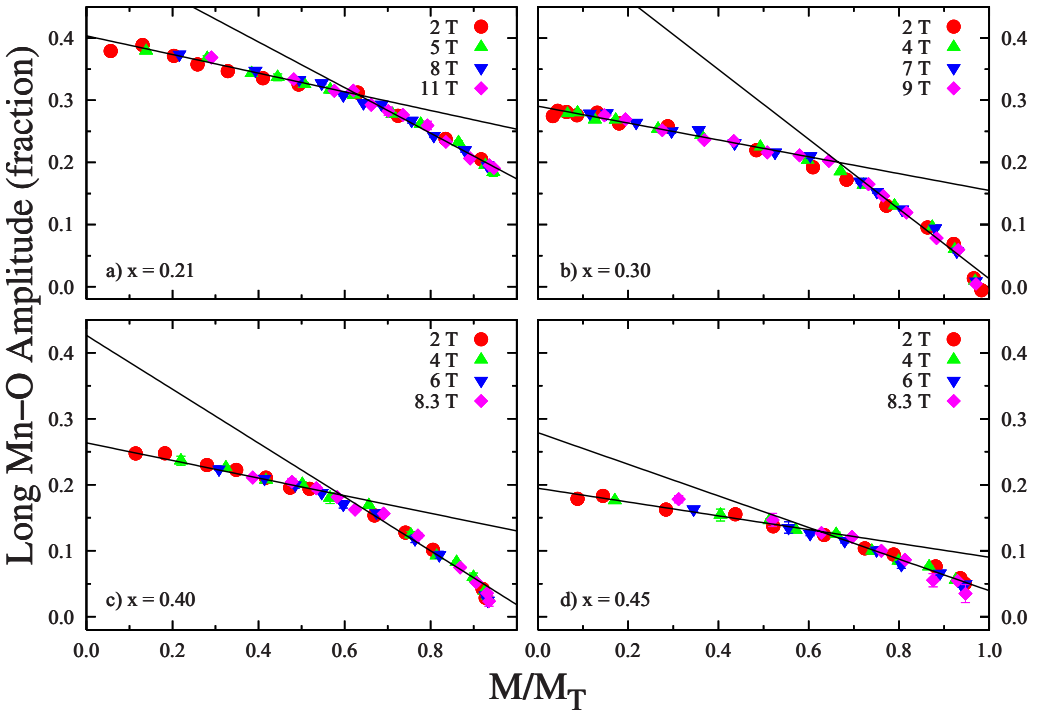

FIG. 17. (Color online) The average Mn-O distortion (modeled by the fraction of long Mn-O bonds) as a function of the fraction of magnetized sites (M/M_T) for the four samples in several applied magnetic fields. The relationship is very similar to Fig. 10 where the average distortion was modeled by the width of the Mn-O distribution function.

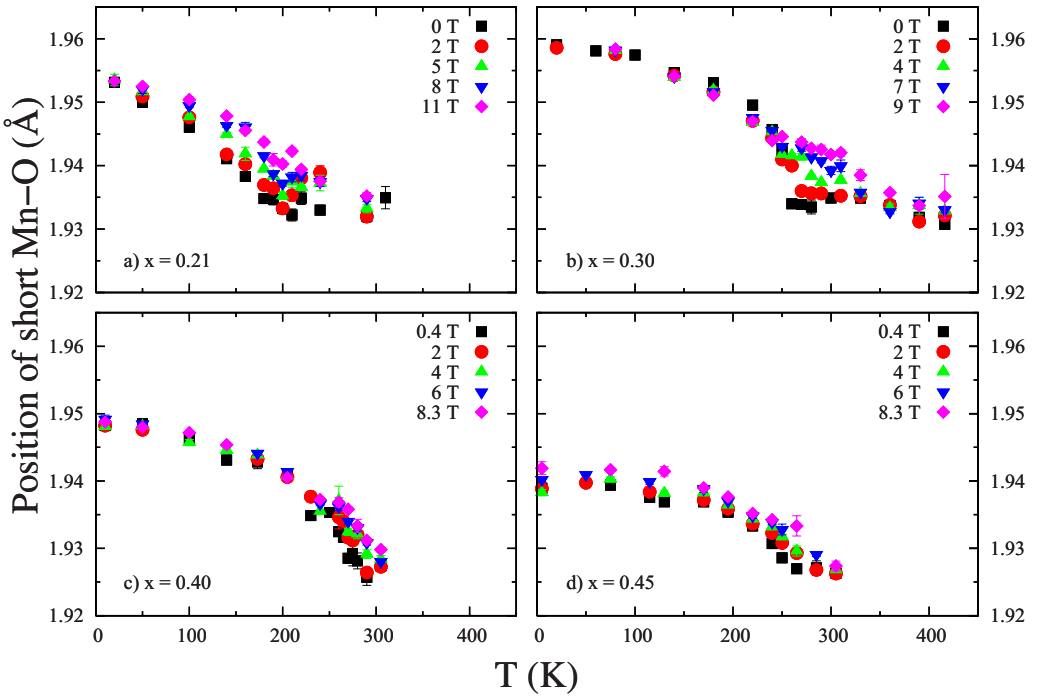

FIG. 18. (Color online) The average length of the short Mn-O bond (i.e., corresponding to the upper portion of Fig. 15) as a function of temperature and magnetic field.

function of applied magnetic field have not been previously observed.

From these detailed fits we also determined the changes in the distance and broadening parameters for the further neighbor peaks. In Sec. III we showed that the Mn-La/Ca peaks are not discernibly affected by the application of an external magnetic field and therefore focus only on the Mn-Mn peak.

The average pair distance and width for the Mn-Mn pair distribution show similar changes as a function of temperature and magnetic field as observed for the nearest neighbor Mn-O distribution but the changes are smaller as shown in Figs. 19 and 20. Note that for the 30% sample (largest T range) the values of r and σ^2 for different B fields overlap quite well, both at low temperature and well above T_c. How-

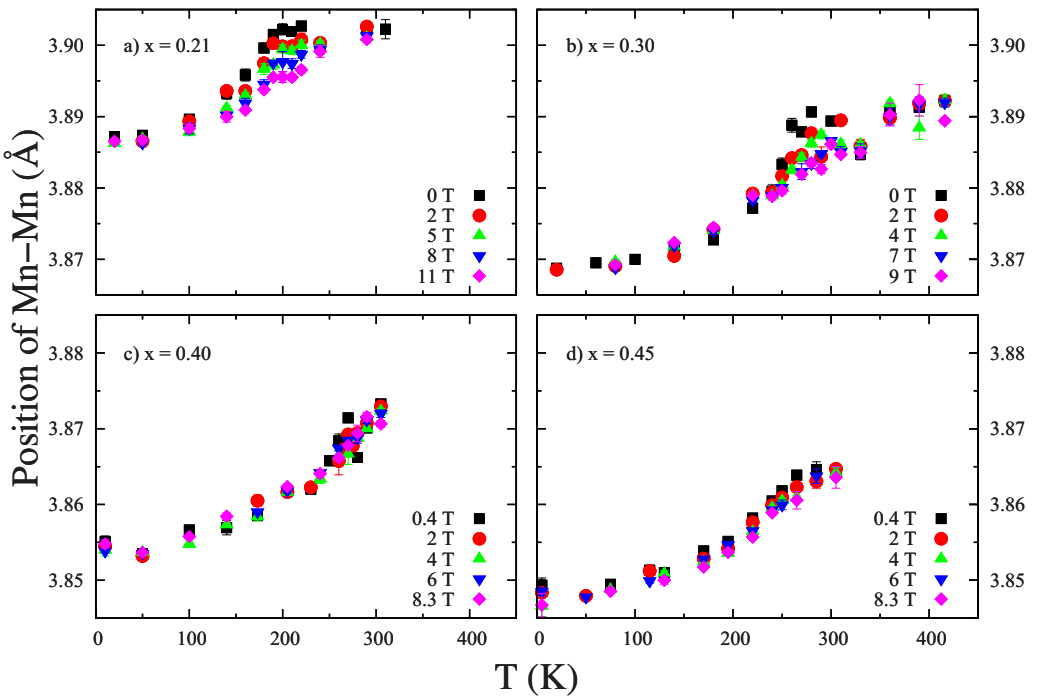

FIG. 19. (Color online) The average position of the Mn-Mn PDF as a function of temperature and magnetic field for each sample.

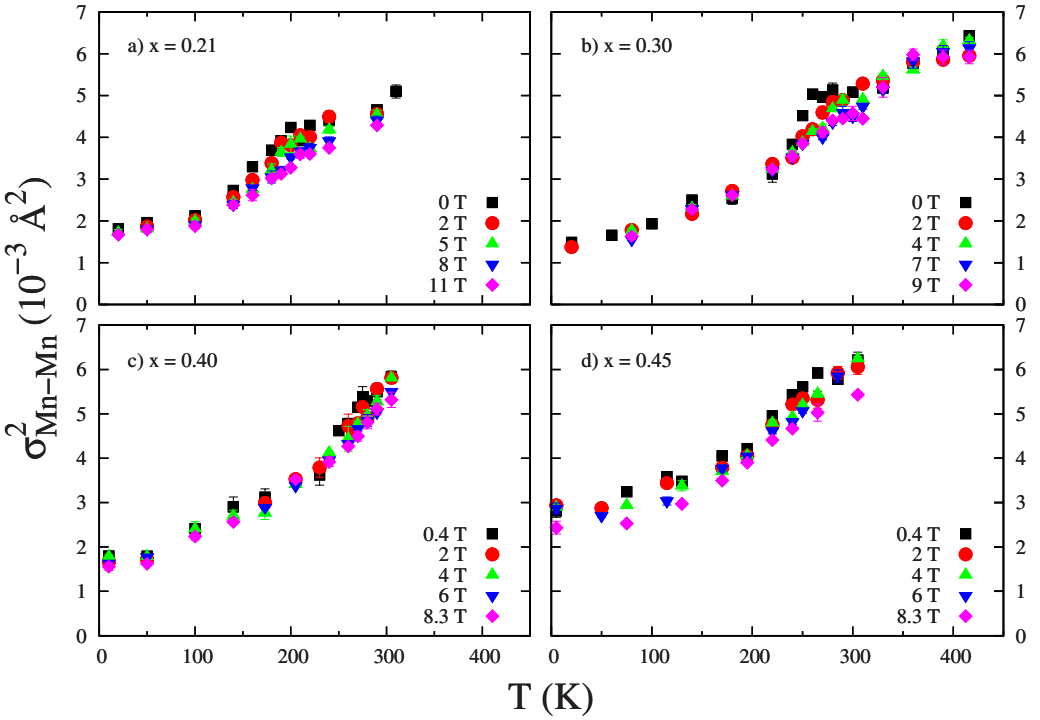

FIG. 20. (Color online) The average width of the Mn-Mn pair-distribution function (PDF) as a function of temperature and magnetic field for each sample.

ever, near T_c, both the average position and σ^2 decrease as a function of the applied magnetic field, although there is considerably more scatter in the Mn-Mn data (compared to the Mn-O data) due to both a reduction in the signal for further neighbors and interference from the Mn-La, Mn-O-Mn, and the Mn-O second neighbor scattering paths that partially overlap the Mn-Mn peak.

The variation of $r_{\text{Mn-Mn}}$ with B field is largest for the 30% and 40% samples near T_c and smallest for the 45% sample. This decrease in the average Mn-Mn distance as the applied magnetic field is increased for T near T_c, provides detailed evidence at the local unit cell level of magnetostriction as a function of temperature and magnetic field in the CMR manganites. The T and B dependences of σ^2 for the Mn-Mn pair is similar to that for the single peak fit to Mn-O but the effect is much smaller; again it is largest for 30% Ca. Similar, field induced changes in the Mn-Mn distribution were also found in high magnetic field XAFS measurements of the melting of the charge/orbitally ordered (C-O) state of $La_{0.5}Ca_{0.5}MnO_3$.[63] Examination of the Mn-O and Mn-Mn correlations revealed three distinct regions in the structure-field diagram: a broad region with weak field dependence (C-O region, disordered), a mixed phase region, and a high field (above 9 T) ferromagnetic phase with low disorder and strong magnetic field-structure coupling.

V. DISCUSSION AND SUMMARY

In the first half of this paper we used a single parameter, σ^2 to parameterize the disorder of the Mn-O PDF. σ^2 includes the effects of split peaks as well as broadening of the PDF from phonons and variations in the JT distortions. A major result from this extensive study of the Mn-O PDF as a function of magnetic field is that there is a direct relationship between distortions of the MnO_6 octahedra and the sample magnetization. Once the thermal phonon contribution is subtracted, and high enough B fields (≥ 2 T) are used such that all magnetic domains are aligned (no domain canting), then there is a *universal* relationship between $\sigma^2_{\text{JT}/polaron}$ and M/M_T (Fig. 10); it is independent of how the magnetization is achieved (i.e., via changes in B and/or T). This universal curve is then a calibration between $\sigma^2_{\text{JT}/polaron}$ and the magnetized fraction; a rather difficult way to measure the magnetization. Because $\sigma^2_{\text{JT}/polaron}$ is not sensitive to canting of the spin moments it can be used as a measure of the fraction of (undistorted) magnetized Mn sites, particularly at low fields, and allows one to see how the bulk magnetization develops in such situations (see Fig. 12). At fields ≤ 0.4 T, the bulk magnetization is generally less than the magnetization determined by the value of $\sigma^2_{\text{JT}/polaron}$. This is not unexpected since canting of domains can be important at low B fields and the magnetization does not quite saturate at low T for $B=0.4$ T for some samples. The transition from partially canted to aligned domains likely occurs below 2 T, probably between 0.4 and 1 T, but we have no data in this range.

At low T (4–20 K) the disorder of the Mn-O bonds is comparable to that for the end compound $CaMnO_3$ for the middle part of the CMR range, roughly $0.25 < x < 0.4$, and $\sigma^2_{\text{Mn-O}}$ is close to the value expected for zero-point motion. For lower concentrations ($x < 0.22$) near the bottom of the CMR range, the distortion at low T increases, likely from $LaMnO_3$-like domains which are not magnetized at low T. At the other end of the CMR range, $x \geq 0.45$, the distortion at low T also increases slightly, possibly from the formation of

a few orbitally ordered domains. However the dominant result at low T within the CMR regime [the ferromagnetic metallic (FMM) phase] is that there is very little disorder of the Mn-O pair distribution function. To make the JT distortions negligible, the holes/electrons must be hopping very fast, much faster than optical phonon time scales; i.e., the time for a hop from one Mn site to another must be significantly shorter than $\sim 10^{-13}$ s. Then the charge carriers are itinerant, the Ca dopants will be screened, and the electron system is relatively homogeneous at the nm scale. Note there can still be a significant electron-phonon interaction[20] as in other systems that do not exhibit the JT effect but the resulting distortions are insignificant compared to the JT distortions observed at high temperatures for the manganites.

The most interesting results are how the JT-type distortions develop and change as a function of T and B. Such distortions are not the same on all sites; Figs. 10 and 11 show that there are clearly two types of distortions present in a given sample at high T near T_c. First there are low distortion sites that have the *same* local distortion for every sample studied. These are the sites that become magnetized first as T is lowered below T_c and must involve the holes since mobile charge carriers are required for the double exchange interaction in the magnetic phase. We therefore associate these low distortion sites with the hopping polarons. An important result of this study is that the fraction of such low distortion Mn sites is found to be significantly larger than the concentration of holes. Thus the polarons must be larger than a single site. Bozin *et al.*[30] also noted that the polarons cannot be localized to a single site and discuss their results in terms of a delocalized polaron picture. Since the same low distortion is present for the polaron sites in all samples, it suggests that there is some stable lowest-energy configuration for the polaron. We refer to the smallest quasiparticle that meets this requirement as the (two-site) dimeron—described in Sec. IA. In this model, if two sites have the same distortion and hence the same JT energy, E_{JT}, but only one electron is present, then hopping between these sites is enhanced. Not all the holes introduced via doping may be associated with low distortion dimerons, and a few, more isolated, slowly hopping, holes may also exist.

In the paramagnetic phase, the local hopping rate will depend on the JT energies on the various Mn sites. For highly distorted sites, E_{JT} will be large and it would cost considerable energy to completely undistort such sites; this is a major barrier for hopping and inhibits the movement of holes into regions with large distortions (low Ca content). At the other extreme, for low distortion dimeron sites with one electron (or one hole) shared between two sites, E_{JT} is small and has the same value for both sites; then locally hopping will be very fast. There may be an intermediate range of distortions within the regions most highly populated by the dimerons. As the dimeron hops through the lattice, a recently occupied dimeron site will have a low distortion for a short time. Then it will be statistically more probable for another nearby dimeron to hop onto this site, instead of a more distorted site. Consequently there may be some lower distortion sites about the dimeron sites—i.e., in the vicinity to the Ca dopants.

The magnitude of E_{JT} at various sites is also important for the onset on FM; from energy arguments alone, one expects that the low distortion sites would become magnetized first. To the extent that most of the dimerons are magnetized first and that they are preferentially located near the Ca dopants, then the conducting magnetic clusters that form just below T_c will be filamentary in nature. If M/M_T is below 0.65, the regions between these conducting filaments will have large distortions and will therefore be nonconducting.

This raises some very important questions which have often been ignored—in the paramagnetic regions, what are the times scales for polaron hopping and for the formation of JT distortions? How long does it takes for a JT distortion to build up when a Mn site becomes occupied by an electron and how fast do the distortions disappear when the site becomes empty? Both of these dynamical processes depend on the motions of the O atoms which move on optical phonon time scales. Thus to significantly reduce the local distortion on Mn sites that are sometimes occupied by electrons, the charge hopping rate must be comparable to phonon frequencies—holes must revisit a given site often enough to inhibit the development of a full JT distortion. Because a low distortion is present for the sites associated with the dimerons—in contrast to a lack of distortion in the magnetic phase—it is unlikely that the local hopping rate in the paramagnetic phase is fast enough that many sites could be coupled and hence only a few (2–4 Mn sites) could be involved.

The second type of distorted sites have larger distortions of the Mn-O PDF and only become magnetized at low T, when $M/M_T > 0.65$ and most of the polaron sites have been incorporated into the magnetic phase. For the lower concentrations, these sites have a very large JT distortion—see the amount of distortion present (i.e., the value of $\sigma^2_{\mathrm{JT}/polaron}$) at the break point in Fig. 10. This quantity decreases rapidly with increasing Ca concentration, and correspondingly, the magnitude of the high slope of the line that describes the high magnetization data, also decreases. This decrease may in part be the consequence of sites with an intermediate distortion, as described above, because the number of such sites should increase with the number of holes added. Surprisingly, as the Ca concentration approaches 0.5, this high slope becomes comparable to the low slope (Fig. 11). Since for $x \sim 0.5$, there are equal numbers of holes and electrons, this supports our proposal that the dimeron corresponds to an electron delocalized over two sites.

The decreased distortion per Mn site in the high M regime at high Ca concentrations means that for these concentrations, the polarons and holes are visiting most Mn sites in times not much longer than the optical phonon period, and e_g electrons do not remain on a given Mn site long enough for a full JT distortion to form. Note that for the $x=0.40$ and 0.45 samples, the fraction of low distortion sites at the break point ($M/M_T \sim 0.65$) is significantly less than twice the hole concentration—thus not all the holes are paired up with a low distortion electron site. Consequently for these samples the slightly higher distortion sites for $M/M_T > 0.65$ are likely a mix of low distortion hole sites and some partially distorted electron sites.

Above T_c (or when $M \sim 0$ in high B fields) the total polaron and JT distortions remain constant up to 400–500 K for the samples we have investigated (see also Ref. 25). Even

though the polarons will hop faster via thermal activation, the local distortions do not change significantly. Neutron-scattering experiments also show a similar result—a small, temperature-independent, structure of order 1 nm in extent[56,57] is observed, that is associated with the individual polarons. To compare these neutron results with the EXAFS, consider a polaron distributed over two Mn sites with low distortions on the associated Mn-O bonds; then the polaron size would be about 0.8 nm. For a polaron covering three Mn sites and the corresponding Mn-O bonds, the size would be $\sim 1.0-1.2$ nm, depending on whether or not the Mn sites were collinear. Thus a polaron that extends over 2–3 Mn sites agrees very well with the neutron scattering results. The EXAFS results show that the local distortions associated with the dimeron are significantly less than the average of distortions for static Mn+3 and Mn+4 sites.

We also fit the Mn-O distribution using two Mn-O peaks to compare with some other analyzes. In this case we used an experimental standard for the Mn-O pair (extracted from $CaMnO_3$) to minimize errors in the theoretical functions and in parameters such as S_o^2. However using a short and a long bond to fit the Mn-O distribution implicitly makes the assumption that there is only one type of JT distortion of the surrounding O octahedra. It does not allow, for example, for a small distortion about a polaron (dimeron) that is different from the large distortion around an isolated Mn+3 site. However as shown in Eq. (5) the total distortion in a two-peak fit is a combination of several parameters—the splittings of the two peaks, the individual σ's, and the ratio of the number of long to short bonds. If one assumes that the main indication of the JT distortion is the number of long bonds, then the T dependence of the short bond peak should be primarily determined by phonon broadening and follow a correlated Debye model. This is the constraint we used in obtaining the fractional number of long bonds as a function of the magnetization shown in Fig. 17. However there is a problem in interpreting this figure, particularly for the 30% Ca concentration. If the slope at high M is representative of a full JT distortion removed from a Mn site when it becomes magnetized, then the greatly reduced slope below $M/M_T \sim 0.6$, would have to correspond to the magnetization of one JT-distorted site for roughly every three undistorted sites—to get an average slope that is about 25% that of the high slope. However there are not enough holes to do so. This inconsistency suggests that one must really consider more than one type of distortion as suggested by the analysis using a single broadening parameter σ. The low slope at low M means that for $M/M_T < 0.6$, about four times as many sites must be magnetized to remove the same amount of distortion as when magnetizing one site at high M. Thus if one assumes that there are some sites with a lower distortion, and hence a shorter long-bond, such that the contribution to the disorder per site is 25% of the full JT distortion, that would explain the data. However a detailed fit of all the bonds for two different types of distorted sites, is not feasible.

Within the two-peak-fit approach, we obtain quite good agreement with recent neutron PDF results[30] but not with other works that suggest that the long Mn-O bond for the CMR regime is longer than 2.1 Å. For temperatures above T_c, and for concentrations from 0.2–0.45, Bozin *et al.*[30] find no bonds with a length above 2.1 Å and at low T the bond lengths collapse to the same length, approximately 1.96 Å. The long bond we find for our two-peak fits is 2.065 ± 0.02 Å. Bozin *et al.* obtain a long bond of 2.07 Å for 21% Ca at 250K and at 550K the long bond varies from about $2.08-2.04$ Å over the CMR range ($0.21 < x < 0.45$).

In addition, for nearly all our data (exception: 21% Ca which still has some distortion at low T) there is very little disorder of the Mn-O distribution in the fully magnetized state, and at 4K the value of σ^2 is low (~ 0.0025 Å^2), close to the value for zero-point motion which is $\sigma^2 \sim 0.0022$ Å^2 for $\theta_{cD} \sim 800$ °C. When there is a split peak there must be an additional static contribution[49] to σ^2 which can be calculated from Eq. (5). For example, for two peaks at 1.92 and 2.01 Å with an amplitude ratio 2:1 and equal σ's, then $\sigma^2_{static} = 0.0018$ Å^2. Then the values of σ^2 in a two-peak fit ($\sigma_1 = \sigma_2$) should be 0.0018 Å^2 lower than obtained in a one-peak fit. However this would suggest a value for $\sigma_1^2 \sim 0.0007$ Å^2 which is far below the value for zero-point motion value and thus unphysically small. The constraint imposed by requiring that σ^2 at low T be equal to or greater than the zero-point-motion value is quite often ignored—in part because data at 20 K or below may not collected or a temperature dependence is not available to estimate θ_{cD}; however it is a very important constraint, and when is not met the model(s) used needs to be reassessed.

For the further neighbor peaks we also find B-field-induced changes in the PDF for the Mn-Mn pair; over the limited range in T for which a large CMR effect and magnetostriction is observed, both the Mn-Mn distance shortens and the disorder in the Mn-Mn PDF decreases with increasing applied field. This variation in the Mn-Mn distance with B field is a direct measure at the unit cell level of the magnetostriction effect. Surprisingly there is no observable change in the Mn-La/Ca peak with increasing B fields—see Figs. 5 and 6; both the average bond length and the broadening of the Mn-La/Ca PDF are unchanged even at the highest B fields. For these temperatures the sample is only partially magnetized and as some of the Mn-Mn distances decrease, the Mn-La/Ca linkage may rotate slightly.

A major result from this extensive study is that the distortions associated with the polarons near and above T_c are significantly smaller than the distortions associated with Mn+3 sites. This is most striking for the lower concentrations within the CMR regime for which the ratio of high and low slopes (Fig. 10) is greater than 4:1. In addition the fraction of low distortion sites—approximately 0.65—is much larger than the concentration of holes and therefore the polarons must cover at least two Mn sites for $x \leq 0.3$. Since the size of the polaron is approximately constant (the low slope is nearly constant—a very slight decrease as x approaches 0.5), we argue that the polaron (dimeron model) covers essentially the same number of sites (~ 2) for the entire CMR range.

In the high T regime, $T > T_c$, the polarons/dimerons move through the sample via hopping but this hopping rate will be much slower than the back-and-forth hopping between two sites that can lead to a reduced distortion for the dimeron. When charge transport takes place via slow polaron hopping, there is less screening of the Ca dopants (which act as nega-

tive charges in the lattice). The polarons will tend to remain near the Ca ions for charge neutrality,[24,42,58] i.e., positively charged polarons in the vicinity of the Ca atoms provide the screening of these dopants. Then for the lower Ca concentrations, the polarons will seldom visit some sites far from a Ca dopant and these sites will have the largest JT distortions. With two general types of distorted sites, the concept of the longer bond becomes diffuse as there may be a distribution of longer bonds.

We should point out that the dimeron model of the polaron is different from many other models; it is a small localized distortion within a lattice which has much larger distortions about the Mn sites. Although similar to Zener's model[6] it includes a distortion, whereas Zener did not. The de Gennes model[8] extends the double exchange interaction to include the spin orientations but also does not explicitly include distortions. Millis *et al.*[9,10] and Röder *et al.*[12] pointed out the importance of JT distortions but neither considered that the distortions about the polarons might be significantly different from the rest of the lattice. Daoud-Aladine *et al.*[64] proposed a modification of Zener's polaron but more for the charge ordered regime—"an ordering of Zener polarons" but they also assumed it had a large JT distortion. However as noted earlier one can also view the charge/orbitally ordered state as an ordered array of dimerons. The pairs of Mn sites in the Daoud-Aladine *et al.* Zener polaron model, have long bonds between them, whereas the pairs of Mn sites in our dimeron model have shorter bonds—the longer bonds are between the dimerons. It is clear that additional calculations are needed to explore cases with quite different and likely time-dependent, local distortions. We hope this detailed study stimulates such theoretical work in the future.

ACKNOWLEDGMENTS

Part of the work at UCSC was supported by NSF under Grant No. DMR0301971 while that at University of Montana (J.J.N.) was supported by NSF under Grant No. DMR0504769. The experiments for $x=0.21$ and 0.3 were performed at SSRL, which is operated by the DOE, Division of Chemical Sciences, and by the NIH, Biomedical Resource Technology Program, Division of Research Resources. Experiments for $x=0.4$ and 0.45 were carried out using the superconducting 10 T x-ray spectroscopy magnet at the National Synchrotron Light Source (NSLS), funded by NSF IMR under Grant No. DMR0083189 (T.A.T.). Use of the NSLS, Brookhaven National Laboratory, was supported by the U.S. Department of Energy, Office of Science, Office of Basic Energy Sciences, under Contract No. DE-AC02-98CH10886.

[1] S. Jin, T. H. Tiefel, M. McCormack, R. Fastnacht, R. M. Fleming, J. Phillips, and R. Ramesh, Science **264**, 413 (1994).
[2] P. Schiffer, A. P. Ramirez, W. Bao, and S.-W. Cheong, Phys. Rev. Lett. **75**, 3336 (1995).
[3] M. Imada, A. Fujimori, and Y. Tokura, Rev. Mod. Phys. **70**, 1039 (1998).
[4] S.-W. Cheong and H. Y. Hwang, in *Colossal Magnetoresistive Oxides*, edited by Y. Tokura (Gordon and Breach, Amsterdam, 2000), Vol. 2, pp. 237–280.
[5] G. H. Jonker, Physica (Amsterdam) **22**, 707 (1956).
[6] C. Zener, Phys. Rev. **82**, 403 (1951).
[7] P. W. Anderson and H. Hasegawa, Phys. Rev. **100**, 675 (1955).
[8] P. G. de Gennes, Phys. Rev. **118**, 141 (1960).
[9] A. J. Millis, P. B. Littlewood, and B. I. Shraiman, Phys. Rev. Lett. **74**, 5144 (1995).
[10] A. J. Millis, B. I. Shraiman, and R. Mueller, Phys. Rev. Lett. **77**, 175 (1996).
[11] A. J. Millis, Phys. Rev. B **53**, 8434 (1996).
[12] H. Röder, J. Zang, and A. R. Bishop, Phys. Rev. Lett. **76**, 1356 (1996).
[13] J. F. Mitchell, D. N. Argyriou, C. D. Potter, D. G. Hinks, J. D. Jorgensen, and S. D. Bader, Phys. Rev. B **54**, 6172 (1996).
[14] P. Norby, I. G. Krogh Andersen, E. Krogh Andersen, and N. H. Andersen, J. Solid State Chem. **119**, 191 (1995).
[15] K. R. Poeppelmeier, M. E. Leonowicz, J. C. Scanlon, and J. M. Longo, J. Solid State Chem. **45**, 71 (1982).
[16] C. H. Booth, F. Bridges, G. J. Snyder, and T. H. Geballe, Phys. Rev. B **54**, R15606 (1996).
[17] T. A. Tyson, J. Mustre de Leon, S. D. Conradson, A. R. Bishop, J. J. Neumeier, H. Röder, and J. Zang, Phys. Rev. B **53**, 13985 (1996).
[18] G. Subías, J. García, M. G. Proietti, and J. Blasco, Phys. Rev. B **56**, 8183 (1997).
[19] C. H. Booth, F. Bridges, G. H. Kwei, J. M. Lawrence, A. L. Cornelius, and J. J. Neumeier, Phys. Rev. Lett. **80**, 853 (1998).
[20] C. H. Booth, F. Bridges, G. H. Kwei, J. M. Lawrence, A. L. Cornelius, and J. J. Neumeier, Phys. Rev. B **57**, 10440 (1998).
[21] A. Lanzara, N. L. Saini, M. Brunelli, F. Natali, A. Bianconi, P. G. Radaelli, and S.-W. Cheong, Phys. Rev. Lett. **81**, 878 (1998).
[22] D. Cao, F. Bridges, C. H. Booth, and J. J. Neumeier, Phys. Rev. B **62**, 8954 (2000).
[23] N. Mannella, A. Rosenhahn, C. H. Booth, S. Marchesini, B. S. Mun, S.-H. Yang, K. Ibrahim, Y. Tomioka, and C. S. Fadley, Phys. Rev. Lett. **92**, 166401 (2004).
[24] L. Downward, F. Bridges, S. Bushart, J. J. Neumeier, N. Dilley, and L. Zhou, Phys. Rev. Lett. **95**, 106401 (2005).
[25] Y. Jiang, F. Bridges, L. Downward, and J. J. Neumeier, Phys. Rev. B **76**, 224428 (2007).
[26] S. J. L. Billinge, R. G. DiFrancesco, G. H. Kwei, J. J. Neumeier, and J. D. Thompson, Phys. Rev. Lett. **77**, 715 (1996).
[27] D. Louca, T. Egami, E. L. Brosha, H. Röder, and A. R. Bishop, Phys. Rev. B **56**, R8475 (1997).
[28] D. Louca and T. Egami, Phys. Rev. B **59**, 6193 (1999).
[29] S. J. L. Billinge, T. Proffen, V. Petkov, J. L. Sarrao, and S. Kycia, Phys. Rev. B **62**, 1203 (2000).
[30] E. S. Božin, M. Schmidt, A. J. DeConinck, G. Paglia, J. F. Mitchell, T. Chatterji, P. G. Radaelli, T. Proffen, and S. J. L. Billinge, Phys. Rev. Lett. **98**, 137203 (2007).
[31] A. I. Abramovich, A. V. Michurin, O. Y. Gorbenko, and A. R.

Kaul, J. Phys.: Condens. Matter **12**, L627 (2000).
[32] A. Abramovich, R. Demin, L. Koroleva, A. Michurin, O. Gorbenko, A. Kaul, R. Szymczak, and B. Krzymanska, Phys. Status Solidi A **189**, 907 (2002).
[33] A. I. Abramovich, L. I. Koroleva, A. V. Michurin, O. Y. Gorbenko, A. R. Kaul, M. K. Mashaev, R. Szymczak, and B. Krzymanska, Phys. Solid State **44**, 927 (2002).
[34] C. Marquina, M. R. Ibarra, A. I. Abramovich, A. V. Michurin, and L. I. Koroleva, J. Magn. Magn. Mater. **226-230**, 999 (2001).
[35] Y. F. Popov, A. M. Kadomtseva, G. P. Vorobev, K. I. Kamilov, V. Y. Ivanov, A. A. Mukhin, and A. M. Balbashov, Phys. Solid State **43**, 1533 (2001).
[36] L. I. Koroleva, R. V. Demin, A. V. Kozlov, D. M. Zashcherinskii, O. Y. Gorbenko, A. R. Kaul, O. V. Melnikov, and Y. M. Mukovskii, J. Magn. Magn. Mater. **316**, e644 (2007).
[37] L. I. Koroleva, R. V. Demin, A. V. Kozlov, D. M. Zashchirinski, and Y. M. Mukovski, J. Exp. Theor. Phys. **104**, 76 (2007).
[38] D. Cao, F. Bridges, D. C. Worledge, C. H. Booth, and T. Geballe, Phys. Rev. B **61**, 11373 (2000).
[39] C. Castellano, F. Cordero, R. Cantelli, C. Meneghini, S. Mobilio, D. D. Sarma, and M. Ferretti, Int. J. Mod. Phys. B **14**, 2725 (2000).
[40] F. Bridges, G. Brown, D. Cao, and M. Anderson, J. Synchrotron Radiat. **8**, 366 (2001).
[41] C. Meneghini, C. Castellano, S. Mobilio, A. Kumar, S. Ray, and D. D. Sarma, J. Phys.: Condens. Matter **14**, 1967 (2002).
[42] J. Alonso, E. Herrero, J. M. Gonzalez-Calbet, M. Vallet-Regi, J. L. Martinez, J. M. Rojo, and A. Hernando, Phys. Rev. B **62**, 11328 (2000).
[43] M. F. Hundley, M. Hawley, R. H. Heffner, Q. X. Jia, J. J. Neumeier, J. Tesmer, J. D. Thompson, and X. D. Wu, Appl. Phys. Lett. **67**, 860 (1995).
[44] M. Jaime, M. B. Salamon, K. Pettit, M. Rubinstein, R. E. Treece, J. S. Horwitz, and D. B. Chrisey, Appl. Phys. Lett. **68**, 1576 (1996).
[45] D. C. Worledge, L. Mieville, and T. H. Geballe, J. Appl. Phys. **83**, 5913 (1998).
[46] M. Y. Kagan, D. I. Khomskii, and M. V. Mostovoy, Eur. Phys. J B **12**, 217 (1999).
[47] T. Kasuya, A. Yanese, and T. Takeda, Solid State Commun. **8**, 1543 (1970).
[48] S. J. L. Billinge (private communication); others have also noted there should be a reduced distortion for polarons in manganites and referred to the distortion about the polaron in $La_{1-x}Sr_xMnO_3$ as an "anti-Jahn-Teller" distortion (Ref. 28), based on the assumption that the hole occupies one site. However our measurements indicate that for $La_{1-x}Ca_xMnO_3$, there is a small distortion associated with the charge carriers and it extends beyond one site.
[49] B. K. Teo, *EXAFS: Basic Principles and Data Analysis* (Springer-Verlag, New York, 1986).
[50] J. A. Victoreen, J. Appl. Phys. **14**, 95 (1943).
[51] J. A. Victoreen, J. Appl. Phys. **19**, 855 (1948).
[52] J. A. Victoreen, J. Appl. Phys. **20**, 1141 (1949).
[53] A. L. Ankudinov, B. Ravel, J. J. Rehr, and S. D. Conradson, Phys. Rev. B **58**, 7565 (1998).
[54] Q. Huang, A. Santoro, J. W. Lynn, R. W. Erwin, J. A. Borchers, J. L. Peng, K. Ghosh, and R. L. Greene, Phys. Rev. B **58**, 2684 (1998).
[55] D. Cao, F. Bridges, M. Anderson, A. P. Ramirez, M. Olapinski, M. A. Subramanian, C. H. Booth, and G. H. Kwei, Phys. Rev. B **64**, 184409 (2001).
[56] J. W. Lynn, D. N. Argyriou, Y. Ren, Y. Chen, Y. M. Mukovskii, and D. A. Shulyatev, Phys. Rev. B **76**, 014437 (2007).
[57] C. S. Nelson, M. v. Zimmermann, Y. J. Kim, J. P. Hill, D. Gibbs, V. Kiryukhin, T. Y. Koo, S.-W. Cheong, D. Casa, B. Keimer, Y. Tomioka, Y. Tokura, T. Gog, and C. T. Venkataraman, Phys. Rev. B **64**, 174405 (2001).
[58] W. Archibald, J.-S. Zhou, and J. B. Goodenough, Phys. Rev. B **53**, 14445 (1996).
[59] Z. Kvitky, F. Bridges, and G. van Dorssen, Phys. Rev. B **64**, 214108 (2001).
[60] This equation is a slight extension of the equation given by Boon Teo (Ref. 49) for the case when the σ's in the two-peak fit are set equal and only the excess width arising from the peak splitting is considered. If one models the pair distribution as the sum of two (or more) Gaussian distributions with different widths, it is straightforward to show that one obtains Eq. (5).
[61] G. Kurczveil, B.S. thesis, University of California, 2006.
[62] E. A. Stern, Phys. Rev. B **48**, 9825 (1993).
[63] T. A. Tyson, M. Deleon, M. Croft, V. G. Harris, C.-C. Kao, J. Kirkland, and S.-W. Cheong, Phys. Rev. B **70**, 024410 (2004).
[64] A. Daoud-Aladine, J. Rodríguez-Carvajal, L. Pinsard-Gaudart, M. T. Fernández-Díaz, and A. Revcolevschi, Phys. Rev. Lett. **89**, 097205 (2002).